Particle based modeling and simulation of natural sand dynamics in the wave bottom boundary layer

Journal:	*Journal of Fluid Mechanics*
Manuscript ID:	Draft
mss type:	Standard
Date Submitted by the Author:	n/a
Complete List of Authors:	Finn, Justin; University of Liverpool, Centre for Engineering Sustainability, School of Engineering Li, Ming; University of Liverpool, Centre for Engineering Sustainability, School of Engineering Apte, Sourabh; Oregon State University, Mechanical Engineering
Keyword:	Particle/fluid flows < Multiphase and Particle-laden Flows, Sediment transport < Geophysical and Geological Flows, Computational methods < Mathematical Foundations

Under consideration for publication in J. Fluid Mech.

Particle based modeling and simulation of natural sand dynamics in the wave bottom boundary layer

Justin R. Finn[1]†, Ming Li[1] and Sourabh V. Apte[2]

[1]Centre for Engineering Sustainability, School of Engineering, the University of Liverpool, Brownlow Street, Liverpool, L69 3GQ, United Kingdom

[2]School of Mechanical, Industrial, and Manufacturing Engineering, Oregon State University, Corvallis, OR 97331, USA

(Received ?; revised ?; accepted ?. - To be entered by editorial office)

Sand transport and morphological change occur in the wave bottom boundary layer due to sand particle interactions with an oscillatory flow and granular interactions between particles. Although these interactions depend strongly on characteristics of the particle population, i.e. size and shape, little is known about how natural sand particles behave under oscillatory conditions, and how variations in particle size influence transport behavior. To enable this to be studied numerically, an Euler-Lagrange point-particle model is developed that can capture the individual and collective dynamics of sub-aqueous natural sand grains. The model is used to simulate sand particle dynamics in two asymmetric oscillatory flow conditions corresponding to the vortex ripple experiments of Van der Werf et al. (*J. Geophysical Research*, vol 112, 2007) and the sheet flow experiments of O'Donoghue and Wright (*Coastal Eng.*, vol 50, 2004). A comparison of phase resolved velocity and concentration fields shows overall excellent agreement between simulation and experiments. The particle based datasets are used to investigate the spatio-temporal dynamics of the particle size distribution and the influence of three dimensional vortical features on particle entrainment and suspension processes. Even for the relatively well sorted medium size sands considered here, the characteristics of the local grain size population exhibit significant space-time variation. Both conditions demonstrate a distinct coarse-over-fine armoring at the bed surface during low velocity phases, which restricts the vertical mobility of finer fractions in the bed, and also results in the strong pickup events involving disproportionately coarse fractions. The near bed layer composition is seen to be very dynamic in the sheet flow condition, while it remains coarse through most of the cycle in the vortex ripple condition. Particles in suspension spend more time sampling the upward directed parts of these flows, especially the smaller fractions, which delays particle settling and enhances the vertical size sorting of grains in suspension. For the sub-millimeter grain sizes considered, most particle-particle collisions occur at low impact Stokes numbers and can be expected to have low rebound velocities.

Key words:

1. Introduction

In a coastal environment, sandy particles on the seabed surface will start to move once the shear force exerted by surface waves and current exceeds critical values. Such

† Email address for correspondence: J.Finn@liv.ac.uk

motion involves complex fluid-particle and particle-particle interactions and can result in various visible features such as vortex ripples in the low flow regime, or a flat bed with intensive transport under large stormy waves, i.e. sheet flows (van Rijn 1993). Increasing evidence from theoretical, experimental and field studies suggest that the physical processes involved in these grain scale interactions often underpin the mechanisms for transport observed on the natural beach. In particular, the size and shape variation of natural sand particles have long been recognized as important factors influencing local sand transport under oscillatory flows. For example, Black & Oldman (1999) observed wave induced grain size sorting and subsequent effects to sand ripple development on the continental shelf, and Vincent *et al.* (1998) and Roos *et al.* (2007) identified spatial variations in the mean grain sizes on the Middelkerke Bank that have clear influences on the sand banks and seabed features along the Belgian coast.

Broadly, grain size influences on transport processes can be classified into two effects. First, for the suspended particles, vertical size sorting and selective transport can lead to very different transport capacity for different size fractions. Especially under oscillatory flows due to surface waves, the strong onshore peak flow under the wave crest can lift a large amount of sand from the bed surface. Once in suspension, the fine fractions take a significant time to settle back to the bed, during which the flow already changes its direction, resulting in enhanced offshore suspended transport, i.e. phase lag effects (Dohmen-Janssen *et al.* 2002). The overall net transport direction for fine sand therefore is often found against the wave propagation direction. In contrast, medium and coarse sands are transported close to the bed by the mean flow, settling during low velocity phases, and their wave-period-averaged net transport tends to be in line with the wave propagation direction (Camenen & Larson 2006; Hassan & Ribberink 2010; Kranenburg *et al.* 2014). Second, within the bed, agitation by the oscillatory shear force together with the bed level changes due to bedform migration or bed scour can lead to inverse size gradation (Legros 2002; Bagnold 1954), where coarse fractions rise to the surface, leaving the finer fractions below with very limited motion. The most noticeable consequence of these armoring and sheltering effects is the shift in transport regime, i.e. a switch from a offshore transport towards an onshore transport or vis versa (Egiazaroff 1965).

Under oscillatory flows, particle exchange between the bedload and suspended load is fairly dynamic through competing settling and entrainment effects (Hassan & Ribberink 2005). Therefore, in order to understand the grain size effects, the transport processes within both the suspension layer and the high concentration bed region need to be examined hand in hand. Yet, most existing model concepts decouple these two regions in some way and largely rely on a single particle representation of the population of natural sand sizes (van Rijn *et al.* 2013). This means that the coupled selective transport in the water column and sorting/segregation phenomena in bed are yet to be fully understood (Blondeaux 2012). Several series of oscillatory flow experiments have provided detailed measurements of net transport rates, flow hydrodynamics, and sediment concentrations for both "uniform" and graded sands in sheet flow conditions (Dohmen-Janssen *et al.* 2002; Ahmed & Sato 2003; O'Donoghue & Wright 2004*a*,*b*; Hassan & Ribberink 2005) as well as above vortex ripples (Fredsøe *et al.* 1999; Van der Werf *et al.* 2007). Due to difficulties involved in measuring individual particle accelerations and grain size while transport is taking place, information about particle dynamics, grain size sorting and the impacts on transport is very limited.

This motivates the development of numerical modeling approaches to identify the mechanisms of grain sorting with relation to the corresponding fluid hydrodynamics. Notable progress has been made by incorporating more physical processes into conventional

advection-diffusion models, such as turbulence closures, granular stress models for the bedload (Hsu *et al.* 2004), and two and three dimensional vortex capturing schemes for rippled beds (Malarkey & Davies 2002; Li & O'Connor 2007). However, the need to understand spatially varying fluid-particle interactions has motivated the development of three dimensional models based on either mixture theory (Penko *et al.* 2010; Ozdemir *et al.* 2010) or discrete particle tracking. In the particle-based approach, hydrodynamic and inter-particle forces acting on the sediment are computed on a per-particle basis, and sediment motion is tracked in a Lagrangian manner. The distinct advantage this approach has over a mixture type model is that multiple particle sizes and natural particle size distributions can be included explicitly without continuum scale closures, allowing grain size dependent transport processes to be captured directly. Early simulations of this type concentrated on bed-load transport of massive particles, where collisional forces are dominant, and one dimensional hydrodynamic models could be justified for the near bed flow (Jiang & Haff 1993; Drake & Calantoni 2001). More recently, increasing computing capacity has sparked an interest in *fully resolved simulation* (FRS), where each particle-fluid interface is represented explicitly and all scales of fluid motion are captured. Impressive results of spherical particle bedload transport in steady currents have been obtained by several groups (Ji *et al.* 2013; Derksen 2011; Kidanemariam & Uhlmann 2014*b*), and the simulations of Kidanemariam & Uhlmann (2014*a*) were able to capture the formation and propagation of small rolling grain and vortex dunes. Although extremely promising in terms of the physical insight provided, FRS of sediment transport will likely be limited to bedload simulations with modest domain sizes and timescales for the foreseeable future because of the computational cost involved.

Application of a particle-based model to study particle size and shape effects important to the natural transport processes of sandy particles has yet been reported in the literature as the authors are aware of. This is due to several important challenges, particularly the effective representation of the wide range of particle sizes and shapes, their interactions with the flow and other grains, and the important interplay between the suspended particles and those in the bed. This paper reports on a new particle based tool to tackle these challenges so that the important particle size effects can be understood. To simulate both bed load and suspended load transport using a particle based model, a compromise must be made between level of detail and computational expense. In this work, an Euler-Lagrange point-particle approach is used, where the particle-fluid interface is not resolved by the continuous phase grid. Instead, particles are treated as point sources of mass and momentum and are coupled to the flow through the appropriately averaged equations (Anderson & Jackson 1967). Collisional forces are computed using a soft-sphere discrete element model (DEM) (Cundall & Strack 1979), while closures for particle-fluid interaction are derived from a combination of theory, experiment and FRS. Such an approach has been widely used by industrial and chemical engineers for some time (Van der Hoef *et al.* 2008), and recent investigations of scour (Hajivalie *et al.* 2012), and current driven boundary layers flows (Schmeeckle 2014) have demonstrated its ability to simulate conditions relevant to coastal sediment transport as well.

A useful assumption to make in a DEM simulation is that the particle shape may be considered spherical, but natural sand particles are quite angular with significant shape variation. When combined with natural size distributions, sand particles can exhibit quite different behavior, both individual and collective, compared to uniform spheres. In particular, the following effects can be regarded as important to consider when designing a particle based model to study natural sand particle dynamics:

(*a*) The packing fraction of a natural sand bed at rest, and its maximum angle of repose both depend strongly on the particle size distribution (Soulsby 1997).

(*b*) The effective drag coefficient on individual angular sand particles is known to be stronger than that of equivalent sized spheres (Fredsøe *et al.* 1992), and there is evidence that the hindered settling velocity of a particle suspension may be influenced by particle shape (Baldock *et al.* 2004).

(*c*) Immersed collisions of sub-aqueous sand particles appear to be more influenced by lubrication forces than collisions of spherical particles (Schmeeckle *et al.* 2001), resulting in lower coefficients of restitution for similarly energetic collisions.

Including realistic size distributions is straightforward, and log-normal size distributions characterized by a median diameter, d_{50}, and geometric standard deviation, σ_g, are used here. Explicit simulation of irregular shaped particles has been performed (e.g. Calantoni *et al.* (2004)), but in the present model it is preferred to retain the computational simplicity of spherical particles and instead irregular shape effects are represented implicitly through several mechanisms in the model equations. The present model builds upon the point-particle approach described by Shams *et al.* (2011); Finn *et al.* (2011); Cihonski *et al.* (2013), extending that model to capture these phenomena in densely laden flows of natural sand grains. The coupled, multiphase equations for Eulerian fluid motion and Lagrangian particle motion are described in Section 2, before addressing, some unique features of their numerical implementation in section 3. The model's ability to predict the individual and collective behavior of sand particles is systematically evaluated in Section 4, before moving to oscillatory flow simulations in Section 5. Simulation results are compared directly with measurements made in both the vortex ripple (Van der Werf *et al.* 2007) and the sheet flow (O'Donoghue & Wright 2004*a*,*b*) regimes, before exploring the size dependent particle motion and spatio-temporal sorting phenomena.

2. Mathematical Model

2.1. *Sediment Motion*

Motion of the sediment phase is computed by evaluating the net force and torque acting on each Lagrangian particle and integrating the following equations for the particle positions, $\boldsymbol{x}_p$, velocities, $\boldsymbol{u}_p$, and angular velocities, $\boldsymbol{\omega}_p$,

$$\frac{d}{dt}(\boldsymbol{x}_p) = \boldsymbol{u}_p, \qquad \frac{d}{dt}(\boldsymbol{u}_p) = \frac{1}{m_p}\sum \boldsymbol{F}_p, \qquad \frac{d}{dt}(\boldsymbol{\omega}_p) = \frac{1}{i_p}\sum \boldsymbol{T}_p, \tag{2.1}$$

where m_p and i_p are the particle mass and moment of inertia respectively. Throughout this work the particle diameter, d_p, is assumed to be on the order of or smaller than the Eulerian grid spacing, Δ. The particle-fluid interface is therefore unresolved and a point-particle formulation is used to model net force, $\boldsymbol{F}_p$, and torque, $\boldsymbol{T}_p$, as a summation of specific hydrodynamic and inter-particle contributions:

$$\boldsymbol{F}_p = \underbrace{\boldsymbol{F}_g}_{Gravity} + \underbrace{\boldsymbol{F}_{pr}}_{Pressure} + \underbrace{\boldsymbol{F}_d}_{Drag} + \underbrace{\boldsymbol{F}_l}_{Lift} + \underbrace{\boldsymbol{F}_{am}}_{Added\ Mass} + \underbrace{\boldsymbol{F}_c}_{Collision} \tag{2.2}$$

$$\boldsymbol{T}_p = \underbrace{\boldsymbol{T}_h}_{Hydrodynamic} + \underbrace{\boldsymbol{T}_c}_{Collision} + \underbrace{\boldsymbol{T}_r}_{Rolling}. \tag{2.3}$$

The formulation of each term is discussed below.

2.1.1. *Hydrodynamic Forces*

Expressions for the hydrodynamic forces and torques acting on individual particles employ closures developed from theory, experiments and fully resolved simulation (FRS).

Force / Torque		Closure
$\boldsymbol{F}_g$	$= -m_p \boldsymbol{g}$	-
$\boldsymbol{F}_{pr}$	$= -\mathcal{V}_p \nabla P_{\|p}$	-
$\boldsymbol{F}_d$	$= m_p \frac{C_d}{\tau_d} (\boldsymbol{u}_{f\|p} - \boldsymbol{u}_p) \frac{d_p}{\langle d \rangle}$	$C_d(Re_p, \Theta_p) = (1-\Theta_p)\left(\frac{C_d(Re_p,0)}{(1-\Theta_p)^3} + A(\Theta_p) + B(Re_p,\Theta_p)\right)$ $A(\Theta_p) = \frac{5.81\Theta_p}{(1-\Theta_p)^3} + 0.48\frac{\Theta_p^{1/3}}{(1-\Theta_p)^4}$ $B(Re_p,\Theta_p) = \Theta_p^3 Re_p\left(0.95 + \frac{0.61\Theta_p^3}{(1-\Theta_p)^2}\right)$ $C_d(Re_p,0) = 1 + 0.15Re_p^{0.687}$ (spheres) $C_d(Re_p,0) = 1.5 + 0.0583Re_p$ (angular sands)
$\boldsymbol{F}_l$	$= m_p C_l \frac{\rho_f}{\rho_p} (\boldsymbol{u}_{f\|p} - \boldsymbol{u}_p) \times (\nabla \times \boldsymbol{u}_f)_{\|p}$	$C_l = \frac{1.61*6}{\pi d_p}\sqrt{\frac{\mu_0}{\rho_f}\left\|(\nabla \times \boldsymbol{u}_f)_{\|p}\right\|}$
$\boldsymbol{F}_{am}$	$= m_p C_{am} \frac{\rho_f}{\rho_p}\left(\frac{D\boldsymbol{u}_{f\|p}}{Dt} - \frac{d\boldsymbol{u}_p}{dt}\right)$	$C_{am} = 0.5$
$\boldsymbol{T}_h$	$= i_p \frac{60}{64\pi}\frac{\rho_f}{\rho_p} C_t \left\|\boldsymbol{\omega}_{rel}\right\| \boldsymbol{\omega}_{rel}$	$C_t = \frac{C_{t1}}{\sqrt{Re_r}} + \frac{C_{t2}}{Re_r} + C_{t3}$ Re_r / C_{t1} / C_{t2} / C_{t3} $Re_r < 1$: 0 / 16π / 0 $1 \le Re_r < 10$: 0 / 16π / 0.0418 $10 \le Re_r < 20$: 5.32 / 37.2 / 0 $20 \le Re_r < 50$: 6.44 / 32.2 / 0 $50 \le Re_r < 100$: 6.45 / 32.1 / 0

TABLE 1. Models for hydrodynamic forces and torques acting on Lagrangian point-particles. The subscript $_{|p}$ denotes a fluid property evaluated at the particle center.

In this work, the total hydrodynamic force acting on each particle contains contributions from gravity, pressure, drag, lift, and added mass effects along the lines of a modified Maxey & Riley (1983) equation for inertial particle motion. When developing system of Lagrangian equations, inclusion or exclusion of individual terms can be justified on a case by case basis, with model closures selected for the desired application. The relatively low specific gravity of marine sediments, and the oscillatory nature of the wave bottom boundary layer have motivated the inclusion of lift and added mass forces, in addition to the more commonly used drag, gravity, and pressure contributions.

The expressions used to compute the hydrodynamic contributions to equations 2.2 and 2.3 are given in Table 1, including closure models where applicable. The equations for hydrodynamic forces and torques require several fluid properties to be interpolated to individual particle locations. The interpolation of fluid property, ϕ_f, from the control volume (CV) centers, $\boldsymbol{x}$ to the particle coordinates $\boldsymbol{x}_p$, is defined,

$$\phi_{f|p} = \sum_{cv} \mathcal{I}(\boldsymbol{x}, \boldsymbol{x}_p)\phi_f, \tag{2.4}$$

where the interpolant function, $\mathcal{I}(\boldsymbol{x}, \boldsymbol{x}_p)$, is a trilinear function that uses the 8 nearest grid points on the three dimensional grid.

The gravity force, $\boldsymbol{F}_g$, is simply the weight of the particle, with g_y taken to be $9.81 m/s^2$

unless otherwise stated. When combined with the pressure force, $\boldsymbol{F}_{pr}$, which involves the gradient of the total fluid pressure, the particles respond to both buoyancy and local variations in dynamic pressure.

The drag force, $\boldsymbol{F}_d$, is computed based on the relative particle velocity,$\left|\boldsymbol{u}_p - \boldsymbol{u}_{f|p}\right|$, the Stokes flow relaxation time, $\tau_d = \frac{\rho_p d_p^2}{18\mu_0}$, and the drag coefficient, $C_d(Re_p, \Theta_p)$. Here, $\Theta_{p|p}$ is the local particle fraction ($\Theta_f = 1 - \Theta_p$ corresponds to the fluid fraction) interpolated to the particle center, and the particle Reynolds number based on the superficial velocity is,

$$Re_p = \frac{\Theta_{f|p}\rho_f d_p \left|\boldsymbol{u}_p - \boldsymbol{u}_{f|p}\right|}{\mu_0}, \tag{2.5}$$

where μ_0 is the dynamic viscosity of the fluid phase without considering effects of the particle suspension (Section 2.2). The functional form of $C_d(Re_p, \Theta_p)$ can significantly influence the collective behavior of particles and is especially important for simulating coastal sediments, where settling velocities can vary by an order of magnitude in the boundary layer due to concentration gradients (Richardson & Zaki 1954). Fully resolved simulations of flow through fixed arrangements of spherical particles have allowed for parametrization of the effective drag coefficient for a wide range of Θ_p and Re_p and recently several relationships for $C_d(Re_p, \Theta_p)$ have been proposed (see Tang *et al.* (2014) for a recent review). For this work, the correlation of Tenneti *et al.* (2011) is chosen for the reason that it has been developed as a correction to the dilute limit, $C_d(Re_p, 0)$, rather than the low Reynolds number limit, $C_d(0, \Theta_p)$. This attribute allows particle shape effects to be more easily incorporated into the drag law by, for example, by specifying the $C_d(Re_p, 0)$ relationship for angular natural sand particles (Fredsøe *et al.* 1992) rather than the typical relation for smooth spherical particles (Schiller 1935). To account for the wide distribution of particle sizes found in naturally graded sands, the polydisperse correction to the drag force proposed by Beetstra *et al.* (2007*a*,*b*) is used. They found that by computing Re_p based on the Sauter mean diameter of the local particle population, $\langle d \rangle$, and scaling the individual particle drag force by a factor $\frac{d_p}{\langle d \rangle}$ provided good results for both bi and polydisperse systems with wide size variations.

Only shear based contributions to the lift force, $\boldsymbol{F}_l$ are considered, and the closure of Saffman (1965) is used for the lift coefficient, C_l. As with the drag closures, new experimental techniques and FRS will hopefully lead to improved relations for C_l in conditions relevant to coastal boundary layers, and future developments can easily be incorporated into the present model. Similarly, investigations of virtual mass effects on particles in non-dilute suspensions should provide improved understanding on how to effectively model the added mass force, $\boldsymbol{F}_{am}$ in these conditions. In the present work, the expression for an isolated rigid sphere in non-uniform flow is used, with added mass coefficient, $C_{am} = 0.5$.

A particle will also experience a hydrodynamic torque, $\boldsymbol{T}_h$, due to its relative rate of rotation in a viscous fluid, $\boldsymbol{\omega}_{rel} = \frac{1}{2}\left(\nabla \times \boldsymbol{u}_f\right)_{|p} - \boldsymbol{\omega}_p$. The expression for $\boldsymbol{T}_h$ contains a torque coefficient, C_t, that is modeled as a function of the particle rotational Reynolds number,

$$Re_r = \frac{\rho_f d_p^2 \left|\boldsymbol{\omega}_{rel}\right|}{4\mu_0}. \tag{2.6}$$

Values of C_t, were determined by Pan *et al.* (2001) by matching the Stokes solution at low Re_r to experimental data at higher Re_r.

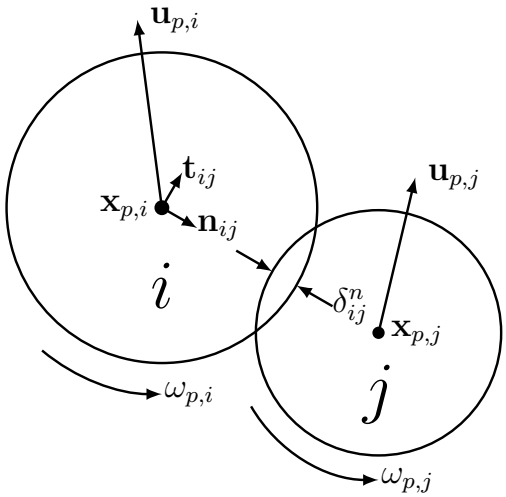

FIGURE 1. Schematic of two particles colliding and the variables used in the soft-sphere collision treatment.

2.1.2. *Particle collisions*

In regions of high particle concentration encountered near the sediment bed, particle motion is dominated by collisions and enduring contacts between particles. To include these collisions in a physically realistic way, a soft-sphere discrete element model (DEM) based on the work of Cundall & Strack (1979) is employed. Figure 1 schematically illustrates a pair of particles, denoted "i" and "j", undergoing collision and the variables used to compute the collision force, $\boldsymbol{F}_c$, collision torque, $\boldsymbol{T}_c$, and rolling torque, $\boldsymbol{T}_r$. During collision a unit normal vector, $\boldsymbol{n}_{ij}$, points from particle i to particle j,

$$\boldsymbol{n}_{ij} = \frac{\boldsymbol{x}_{p,j} - \boldsymbol{x}_{p,i}}{|\boldsymbol{x}_{p,j} - \boldsymbol{x}_{p,i}|}. \tag{2.7}$$

In order to mimic the elastic deformation that occurs during collision, the two colliding particles are allowed to overlap slightly in the normal direction, by an amount

$$\delta_{ij}^n = 0.5\left(d_{p,i} + d_{p,j}\right) - \left|\boldsymbol{x}_{p,i} - \boldsymbol{x}_{p,j}\right|. \tag{2.8}$$

The total relative velocity of the two spheres at the contact point can be written as

$$\boldsymbol{u}_{ij} = \boldsymbol{u}_{p,i} - \boldsymbol{u}_{p,j} + \left(\frac{1}{2}d_{p,i}\boldsymbol{\omega}_{p,i} + \frac{1}{2}d_{p,j}\boldsymbol{\omega}_{p,j}\right) \times \boldsymbol{n}_{ij}, \tag{2.9}$$

and can be decomposed into the normal and tangential components,

$$\boldsymbol{u}_{ij}^n = \left(\boldsymbol{u}_{ij} \cdot \boldsymbol{n}_{ij}\right)\boldsymbol{n}_{ij} \tag{2.10}$$

$$\boldsymbol{u}_{ij}^t = \boldsymbol{u}_{ij} - \boldsymbol{u}_{ij}^n. \tag{2.11}$$

The normal force generated by the collision is modeled by considering the overlapping particles as a linear spring-damper system, with spring constant, k_n and damping constant, ξ_n.

$$\boldsymbol{F}_{c,ij}^n = \begin{cases} -k_n\delta_{ij}\boldsymbol{n}_{ij} - \xi_n\boldsymbol{u}_{ij}^n & \text{for: } |\boldsymbol{x}_{p,i} - \boldsymbol{x}_{p,j}| < 0.5\left(d_{p,i} + d_{p,j}\right) + \alpha \\ 0 & \text{otherwise} \end{cases} \tag{2.12}$$

In the equation above the parameter α is the so called *radius of influence* (Patankar &

Joseph 2001). Values of α greater than zero will initiate a repulsive force slightly before the particles overlap. This allows the model to be robust for high speed collisions, but will result in close-packed states that are less dense than in real systems. To achieve correct close packing densities, α is adjusted linearly as a function of the collision CFL number (Capecelatro & Desjardins 2012),

$$\alpha = \frac{\alpha_0}{2}\left(d_{p,i}+d_{p,j}\right)\left(\frac{CFL^c_{ij}}{CFL^c_{max}}\right), \text{ where } \quad CFL^c_{ij} = \frac{2\left|\boldsymbol{u}_{ij,n}\right|\Delta t_p}{\left(d_{p,i}+d_{p,j}\right)}. \tag{2.13}$$

Here, Δt_p is the particle timestep and α_0 is the maximum radius of influence, which is used when the collision CFL is equal to the maximum permitted collision CFL number, CFL^c_{max}.

A similar linear spring-damper analogy with the addition of a frictional limiter is used to model the frictional forces generated by relative motion in the tangential direction as,

$$\boldsymbol{F}^t_{c,ij} = \begin{cases} -k_t\boldsymbol{\delta}^t_{ij} - \xi_t\boldsymbol{u}^t_{ij} & \text{for: } \left|k_t\boldsymbol{\delta}^t_{ij}\right| \le \vartheta_s\left|\boldsymbol{F}^n_{c,ij}\right|, \left|\boldsymbol{F}^n_{c,ij}\right| > 0 \quad \text{(sticking)} \\ -\vartheta_s\left|\boldsymbol{F}^n_{c,ij}\right|\boldsymbol{t}_{ij} & \text{for: } \left|k_t\boldsymbol{\delta}^t_{ij}\right| > \vartheta_s\left|\boldsymbol{F}^n_{c,ij}\right|, \left|\boldsymbol{F}^n_{c,ij}\right| > 0 \quad \text{(sliding)} \\ 0 & \text{for: } \left|\boldsymbol{F}^n_{c,ij}\right| = 0 \quad \text{(no contact)} \end{cases} \tag{2.14}$$

Here, ϑ_s is the coefficient of static/sliding friction, and the tangential unit vector is defined from the extension of the tangential spring, $\boldsymbol{t}_{ij} = \frac{\boldsymbol{\delta}^t_{ij}}{\left|\boldsymbol{\delta}^t_{ij}\right|}$. The model distinguishes between the sticking and sliding regimes based on the tangential displacement history, a feature crucial to obtaining stable heap formation (Brendel & Dippel 1998). This requires storing and updating the length of the tangential spring, $\boldsymbol{\delta}^t_{ij}$ during each timestep according to,

$$\boldsymbol{\delta}^t_{ij} = \begin{cases} \boldsymbol{\delta}^t_{ij} + \boldsymbol{u}^t_{ij}\Delta t_p & \text{(sticking)} \\ -\frac{1}{k_t}\left(\vartheta_s\left|\boldsymbol{F}^n_{ij}\right| + \xi_t\boldsymbol{u}^t_{ij}\right) & \text{(sliding)} \\ 0 & \text{(no contact)} \end{cases} \tag{2.15}$$

Because the tangential plane may change during the duration of the contact, the length of the spring is projected back into the current tangential plane after every step as,

$$\boldsymbol{\delta}^t_{ij} = \boldsymbol{\delta}^t_{ij} - \left(\boldsymbol{\delta}^t_{ij}\cdot\boldsymbol{n}_{ij}\right)\boldsymbol{n}_{ij}. \tag{2.16}$$

The total force acting on particle i due to collision with all other particles j is then,

$$\boldsymbol{F}_c = \sum_{j/=i} \boldsymbol{F}^n_{c,ij} + \boldsymbol{F}^t_{c,ij}, \tag{2.17}$$

and from Newton's third law it follows that $\boldsymbol{F}_{c,ji} = -\boldsymbol{F}_{c,ij}$. The corresponding collisional torque on particle i is due to the tangential collision forces described above,

$$\boldsymbol{T}_c = \sum_{j/=i} \frac{d_i}{2}\boldsymbol{F}^t_{c,ij}\times\boldsymbol{n}_{ij} \tag{2.18}$$

We also include a rolling torque to account for the increased rolling resistance of irregularly shaped particles, and use the directional constant torque model of Zhou *et al.* (1999*b*),

$$\boldsymbol{T}_r = \sum_{j/=i} -\vartheta_r\left|\boldsymbol{F}^n_{c,ij}\right| r_{ij}\frac{\boldsymbol{\omega}_{rel}}{\left|\boldsymbol{\omega}_{rel}\right|}. \tag{2.19}$$

Here, ϑ_r is the non-dimensional coefficient of rolling friction, $r_{ij} = \frac{1}{2}\frac{d_i d_j}{d_i+d_j}$ is the reduced radius, and $\boldsymbol{\omega}_{rel} = \boldsymbol{\omega}_{p,i} - \boldsymbol{\omega}_{p,j}$ is used to form a unit vector in the direction of rolling resistance for particle i.

2.2. *Fluid Motion*

The discrete Lagrangian sediment motion is coupled to the continuous Eulerian fluid motion by solving the volume filtered Navier-Stokes equations (Anderson & Jackson 1967; Cihonski *et al.* 2013)

$$\frac{\partial}{\partial t}(\rho_f \Theta_f) + \nabla \cdot (\rho_f \Theta_f \boldsymbol{u}_f) = 0 \tag{2.20}$$

$$\frac{\partial}{\partial t}(\rho_f \Theta_f \boldsymbol{u}_f) + \nabla \cdot (\rho_f \Theta_f \boldsymbol{u}_f \boldsymbol{u}_f) =$$
$$-\nabla p + \nabla \cdot \left(\mu_{eff} \left(\nabla \boldsymbol{u}_f + \nabla \boldsymbol{u}_f^T - \frac{2}{3} \nabla \cdot \boldsymbol{u}_f \right) \right) - \Theta_f \rho_f \boldsymbol{g} + \boldsymbol{f}_{p \to f} \tag{2.21}$$

In the above form the conservation equations account for the volume of fluid which is locally displaced by the motion of the sediment through the fluid fraction, Θ_f. In addition to volume exclusion effects, Eqn. 2.21 also contains the typical interphase momentum transfer term, $\mathbf{f}_{p \to f}$. This term includes the equal and opposite reaction from the particle surface forces back to the flow. To define these quantities, it is necessary to introduce the filter operation which distributes a property of the particles, ϕ_p, to the continuous field, ϕ_f, located at the Eulerian grid points,

$$\phi_f(\boldsymbol{x}) = \sum_{i_p=1}^{n_p} \mathcal{F}(\boldsymbol{x}, \boldsymbol{x}_p) \phi_p. \tag{2.22}$$

The truncated polynomial filter function, $\mathcal{F}$, suggested by Deen *et al.* (2004) is used,

$$\mathcal{F}(\boldsymbol{x}, \boldsymbol{x}_p) = \begin{cases} \frac{15}{16} \left[\frac{|\boldsymbol{x} - \boldsymbol{x}_p|^4}{\sigma^5} - 2 \frac{|\boldsymbol{x} - \boldsymbol{x}_p|^2}{\sigma^3} + \frac{1}{\sigma} \right] & |\boldsymbol{x} - \boldsymbol{x}_p| < \sigma \\ 0 & \text{otherwise,} \end{cases} \tag{2.23}$$

where σ is the filter width that controls the region of influence of each particle, and is set to $3d_{50}$ for all simulations in this work. Using Equations 2.22 and 2.23, the fluid fraction of a control volume with volume $\mathcal{V}_{cv}$ is defined from the particle positions as,

$$\Theta_f(\boldsymbol{x}) = 1 - \frac{1}{\mathcal{V}_{cv}} \left[\sum_{i_p=1}^{n_p} \mathcal{F}(\boldsymbol{x}, \boldsymbol{x}_p) \frac{\pi}{6} d_p^3 \right]. \tag{2.24}$$

Similarly, the interphase momentum transfer term is,

$$\mathbf{f}_{p \to f}(\boldsymbol{x}) = - \sum_{i_p=1}^{n_p} \mathcal{F}(\boldsymbol{x}, \boldsymbol{x}_p) (\mathbf{F}_{pr} + \mathbf{F}_d + \mathbf{F}_l + \mathbf{F}_{am}). \tag{2.25}$$

The variation of the effective viscosity of the sediment-fluid suspension is modeled using the formulation of Eilers (1941) as,

$$\mu_{eff} = \mu_0 \left[1 + \frac{0.5 [\mu] \Theta_p}{(1 - \Theta_p) / \Theta_{cp}} \right]^2 \tag{2.26}$$

Here, $\Theta_{CP} \approx 0.6$ is the close packed solid fraction, and $[\mu]$ is the *intrinsic viscosity* which accounts for the effect of particle shape on the rheology of the mixture. Following the recommendations of Penko *et al.* (2009), $[\mu] = 2.5$ for spherical particles, and $[\mu] = 3.0$ for natural sands.

Unresolved, sub-grid scale turbulent stresses can be modelled using a large eddy simulation approach, thereby adding a turbulent contribution to μ_{eff} (Shams *et al.* 2011).

In the conditions considered here, the flow is resolved at near particle scale, and this contribution has been confirmed to be minor.

3. Numerical Implementation

The two systems of equations for the particles (eq: 2.1-2.3) and fluid (Equation 2.20-2.21) are coupled and solved in a structured, Cartesian grid framework using a finite volume discretization and a pressure-based, second-order, fractional time-stepping scheme based on the work of Shams *et al.* (2011) and Cihonski *et al.* (2013). Below elements of the implementation unique to natural sand boundary layer simulation are discussed, namely justification of collision parameter values, and particle time advancement strategy.

3.1. *Collision parameters*

The particle collision model contains eight parameters, namely k_n, k_t, ξ_n, ξ_t, α_0, CFL^c_{max}, ϑ_s, and ϑ_r, that can potentially influence both the micro and macro-scale particle behavior. In selecting values for them, the goal is achieve physically meaningful results while maximizing speed and numerical stability of the model. From a numerical standpoint, the main challenge is selecting an appropriate value for the normal particle stiffness, k_n. It is possible to derive values for k_n and k_t directly from the Young's and Shear moduli of a material, but such values can result in prohibitively small contact durations, $\tau_c \propto \sqrt{m_p/k_n}$, which must be resolved by the simulation particle timestep, Δt_p. Arguably, bulk particle motion will be rather insensitive to variations in stiffness in the presence of large dissipative forces (ie. drag), and this has been observed to be true in prior numerical studies (ie Drake & Calantoni (2001)). In general, k_n is chosen to be large enough to avoid significant particle overlap ($> 1\%$) rather than correspond to material stiffness.

The ratio of tangential stiffness to normal stiffness is set to a value of $k_t/k_n = 0.4$ for all simulations unless otherwise stated. To compute the radius of influence, $\alpha_0 = 0.075$ and $CFL^c_{MAX} = 0.1$, in line with Patankar & Joseph (2001) and Capecelatro & Desjardins (2012).

For most materials the dry coefficient of normal restitution, $e_{n,dry}$, is well characterized, and can be used to relate the normal damping parameter, ξ_n to the spring constant k_n through an analytical solution to the linear mass-spring-damper problem,

$$\xi_n = \frac{-2 \ln e_n \sqrt{m_{ij} k_n}}{\sqrt{\pi^2 + \ln^2 e_n}}, \tag{3.1}$$

where e_n is taken to be $e_{n,dry}$ and $m_{ij} = \frac{m_i m_j}{m_i + m_j}$ is the reduced mass. During the rebound phase of an immersed (wet) collision, the flow in the gap between two particles may result in a significantly suppressed rebound velocity, and lower effective coefficient of restitution, $e_{n,wet}$. Point-particle models that do not resolve this flow need to model the effects of these unresolved lubrication forces. Controlled experiments (Joseph *et al.* 2001; Schmeeckle *et al.* 2001) and FRS (Simeonov & Calantoni 2012) have demonstrated the strong dependence of $e_{n,wet}$ on the impact Stokes number,

$$St = \frac{m_{ij} \left| \boldsymbol{u}^n_{ij} \right|}{6\pi\mu_0 r^2_{ij}}, \tag{3.2}$$

showing that there is a limit, St_c, below which no rebound occurs ($e_{n,wet} = 0$) and an elastic limit, St_e, above which the rebound is unaffected by lubrication forces ($e_{n,wet} = e_{n,dry}$). Based on the observations of Schmeeckle *et al.* (2001) for natural sand grain

impacts, it is assumed that $e_{n,wet}$ varies linearly with St for impacts in the transition range ($St_c < St < St_e$),

$$e_{n,wet} = \min\left[\max\left[\frac{St - St_c}{St_e - St_c}, 0\right], 1\right] e_{n,dry}. \tag{3.3}$$

Similar to the tangential spring history, $e_{n,wet}$ is computed during the initiation of contact between two particles and stored as a property of the collision pair, ij, for the duration of each contact. It is then used in equation 3.1 to compute ξ_n. Tangential damping effects are neglected by setting $\xi_t = 0$.

Values for the friction coefficients ϑ_s and ϑ_r may be determined experimentally for spherical particles, but the frictional interactions between angular sand grains are more difficult to characterize. Ideally the model should be able to match the collective behavior of angular sand particles, especially the close packing fraction and angle of repose, while retaining a spherical representation for numerical convenience. To accomplish this, the influence of ϑ_s and ϑ_r on these two parameters are studied in Section 4.2 for spherical particles with a lognormal size distribution. This leads to the choice of $\vartheta_s = 0.4$ and $\vartheta_r = 0.06$ for all subsequent simulations of natural sand behavior.

3.2. *Particle time advancement*

For the sub-millimeter particle sizes considered here, collision durations can be quite small relative to the required fluid timestep, and sub-cycling of the particle equations (2.1-2.3) is performed with $\Delta t_p << \tau_c$. Simulations of purely granular systems often employ high-order schemes for accurate particle time advancement, but in the presence of large dissipative forces (drag), first order schemes perform adequately with low computational overhead (Van der Hoef *et al.* 2008; Shams *et al.* 2011), and first order Euler time advancement is used here.

Simulating bedforms with a particle based approach can be very computationally intensive due to the severe separation of space and timescales: Vortex sand ripples are typically tens of centimeters in length, meaning several million particles can be needed to simulate both bed-load and suspended load over a single ripple. When combined with the short collision durations, solving the particle equations can quickly become a simulation bottleneck. To address this issue and enable the model to simulate full scale bedforms, the model performs an extra step to identify which grains may be mobilized by the flow at any given instant. The concept is similar in spirit to the "bottom to top reconstruction" methods sometimes use to simulate static granular assemblies (Pöschel & Schwager 2005) and is illustrated in Figure 2. At regular intervals, the location of the three dimensional bedform surface is computed by finding the level-set $\Theta_p = 0.5$. Each particle is then classified based on its depth, $\mathcal{D}$ below this interface as either *mobile* ($\mathcal{D} < 9d_{50}$), *fixed* ($9d_{50} < \mathcal{D} < 18d_{50}$), or *dormant* ($18d_{50} < \mathcal{D}$). Particle motion is then updated according to this classification as follows:

- **Mobile**: The particle is mobile, and will be advanced according to system 2.1, using the time-step $\Delta t_p << \tau_c$.
- **Fixed**: $\boldsymbol{u}_p$ and $\boldsymbol{\omega}_p$ are set to zero, but all forces acting on the particle are computed with the same Δt_p as for mobile particles.
- **Dormant**: $\boldsymbol{u}_p$ and $\boldsymbol{\omega}_p$ are set to zero, and only hydrodynamic forces are computed, with a larger timestep equal to Δt_f (no sub-cycling).

If the number of dormant particles at any instant is large, the strategy described here becomes very efficient without sacrificing the ability to capture particle-fluid coupling and associated morphological change (i.e. ripple migration).

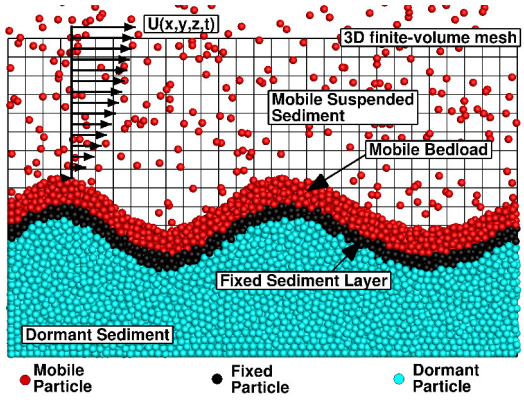

FIGURE 2. Strategy for isolating mobile grains on the surface of bedforms during the simulation.

4. Model Validation and Calibration

Extensive validation of the method for dilute bubble and particle laden flows has been reported elsewhere (Shams *et al.* 2011; Finn *et al.* 2011; Cihonski *et al.* 2013). In this section, the model is validated and calibrated for simulating sub-aqueous natural sand behavior, namely (i) immersed collision dynamics, (ii) macroscale packing fraction and angle of repose, and (iii) hindered settling behavior at both dense and dilute concentrations.

4.1. *Immersed Collision Behavior*

Simeonov & Calantoni (2012) highlighted the importance of unresolved lubrication forces when simulating immersed particle collisions. Using an FRS approach with grid resolutions up to $d_p/\Delta = 64$, and a microscale lubrication and cavitation model, they successfully reproduced the experimentally observed dependence of the normal and tangential coefficients of restitution on the impact Stokes number for oblique binary collisions of spherical particles. Their tests are repeated here to evaluate the present unresolved point-particle collision and lubrication model.

Two spherical particles, a "projectile" and a "target", each with diameter, $d_p = 2$mm and $\rho_p = 6000\text{kg/m}^3$ are initially at rest and offset by a distance (X_{off}, Y_{off}) in the XY plane, as shown in Figure 3a. To obtain different angles of incidence, X_{off} is varied from 0.1mm to 1.9mm, in steps of 0.1mm, while $Y_{off} = 6$mm is held constant. A uniform acceleration of $g_y = 51.4\text{mm/s}^2$ is applied to the projectile particle. The mechanical contact parameters, summarized in Table 2, are chosen to be as close as possible to the FRS despite the somewhat different model for normal force used by Simeonov & Calantoni (2012). The dry coefficient of restitution is set to $e_{n,dry} = 0.97$, and the lubrication model parameters are set to $St_c = 11$ and $St_e = 130$, corresponding to the range of mostly damped to mostly elastic collisions for spherical particles (Yang & Hunt 2006). Two sets of tests are run for dry ($\rho_f = 1 \times 10^{-5}$ kg/m^3, $\mu_0 = 1 \times 10^{-10}$ kg/m$-$s) and wet ($\mu_0 = 1 \times 10^{-3}$ kg/ms, $\rho_f = 1 \times 10^3$ kg/m^3) collisions. The flow is solved on a regular grid with $\Delta = d_p$ using a timestep $\Delta t_f = 3 \times 10^{-4}$ s, while the particles are updated using $\Delta t_p = 5 \times 10^{-6}$ s.

The impact Stokes number for the wet collision simulations is in the range $18 \lesssim St \lesssim 45$, meaning lubrication effects are important. In Figure 3b, the angles of incidence and recoil are plotted for both dry and wet collisions alongside the FRS results of Simeonov

d_p	ρ_p	k_n	k_t	e_{dry}	St_c	St_e	$\mathcal{V}_s$	$\mathcal{V}_r$	Δt_p	α_0
2 mm	6000kg/m^3	10,000 N/m	7000 N/m	0.97	11	130	0.25	0.0	5e-6 s	0.075

TABLE 2. Particle parameters used for the oblique binary collision tests.

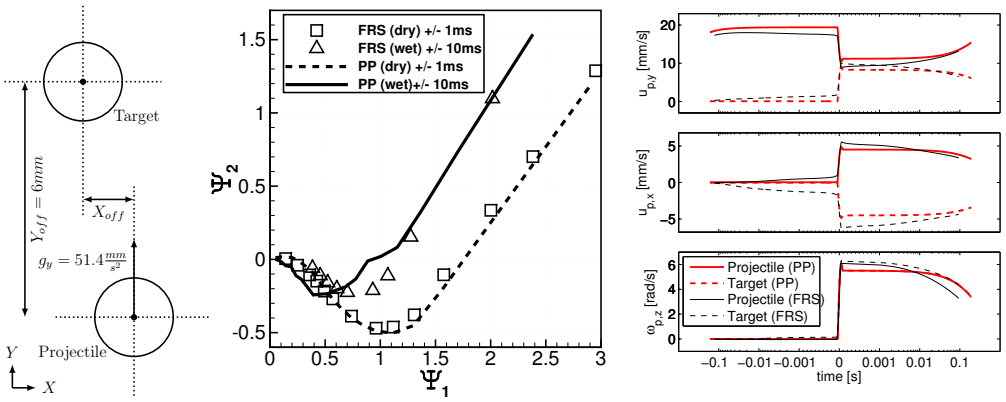

(a) (b) (c)

FIGURE 3. Comparison of oblique binary collisions with the FRS results of Simeonov & Calantoni (2012). (a) shows the problem configuration. (b) is a plot of the tangent of the recoil angle, Ψ_2, vs the tangent of the incidence angle, Ψ_1, for both wet and dry collisions. (c) Compares trajectories pre-and post collision predicted by the FRS and the present point-particle models.

& Calantoni (2012). The angles are measured using their tangents,

$$\Psi_1 = -\frac{\boldsymbol{u}_{ij} \cdot \boldsymbol{t}_{ij}}{\boldsymbol{u}_{ij} \cdot \boldsymbol{n}_{ij}}, \text{ and } \Psi_2 = -\frac{\boldsymbol{u}'_{ij} \cdot \boldsymbol{t}_{ij}}{\boldsymbol{u}_{ij} \cdot \boldsymbol{n}_{ij}}, \tag{4.1}$$

Where $\boldsymbol{u}_{ij}$ and $\boldsymbol{u}'_{ij}$ are the total relative velocities at the contact point before and after the collision respectively, and the unit normal and tangential vectors are assumed not to vary significantly during the contact. For comparison with the FRS, $\boldsymbol{u}_{ij}$ and $\boldsymbol{u}'_{ij}$ are evaluated at $\pm$ 1ms for the dry collisions and $\pm$ 10ms for the wet collisions. The point-particle model combined with the linear model for e_{wet} (Equation 3.3) reproduces the main features of the FRS results quite well, for both dry and wet collisions.

A more detailed comparison of the FRS and point-particle velocities before and after impact is made in Figure 3c, for the X_{off}=1.3mm case. For direct comparison with FRS, all results are plotted with $t = 0$ corresponding to the time of maximum normal overlap. The post-collision behavior of velocity components are in good agreement with the FRS and the point-particle model for hydrodynamic torque faithfully predicts the post-collision decay of angular velocity for the projectile and target in the mostly irrotational background flow. The main observable difference is that the target particle in the FRS acquires a significant velocity before mechanical contact occurs while the projectile slows during its approach. This is due to resolved pressure gradients in the gap between the two particles, which cannot be captured by a point-particle model. For small offsets, this motion results in increased values of Ψ_1, and explains the difference between the FRS and point-particle trend for wet collisions in Figure 3b.

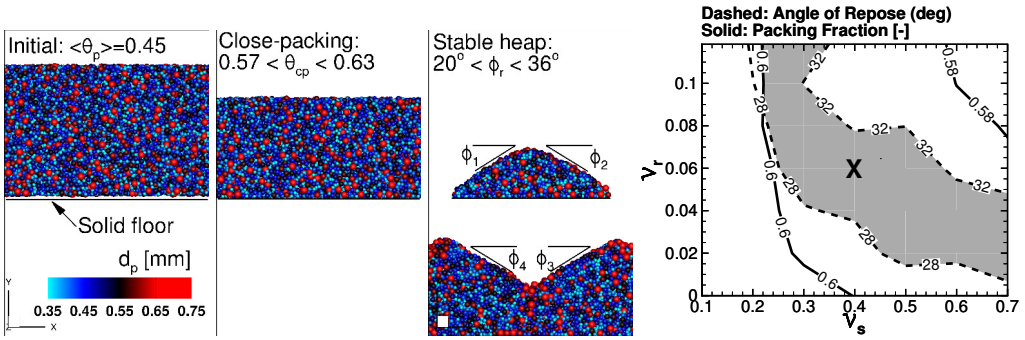

FIGURE 4. Simulation of random close packing and heap formation. (a) Particles are seeded at random. (b) The particles settle under the action of gravity in quiescent water until they reach a close packed state with density Θ_{cp}. (c) An avalanche is initiated by removing a portion of the floor, and the mean angle of repose is measured once the heap has stabilized. (d) Contour plot of packing fraction and angle of repose as a function of friction coefficients. The shaded region corresponds to acceptable friction coefficients for natural sands using the present model.

d_{50}	σ_g	ρ_p	k_n	k_t	e_{dry}	St_c	St_e	$\mathcal{V}_s$	$\mathcal{V}_r$	Δt_p
0.51mm	1.28	2650 kg/m^3	1,000 N/m	400 N/m	0.6	39	105	0.1-0.7	0.0-0.12	1.5e-6 s

TABLE 3. Collision parameters used for the close-packing and avalanching tests.

4.2. *Packing Fraction and Angle of Repose*

In addition to binary interactions, the model must also capture the collective behavior of natural sand grains, namely the close packing density, Θ_{cp}, and the angle of repose, ϕ_r, to predict particle dynamics within the bed. In nature, these properties typically depend on the degree of size sorting and bed compaction (Soulsby 1997), and for the average to well sorted ($d_{84}/d_{16} \lesssim 2$) quartz sands considered here, it is expected that $0.58 \lesssim \Theta_{cp} \lesssim 0.6$ and $28^o \lesssim \phi_r \lesssim 32^o$ under average compaction. The coefficients of sliding and rolling friction, ϑ_s and ϑ_r are the main model parameters that influence these properties in spherical particle DEM simulations (Zhou *et al.* 1999*b*), and a combined packing and avalanching test was performed in order to calibrate the model to mimic the behavior of natural sands.

A three dimensional domain was seeded with 21,370 randomly positioned non-overlapping spheres to obtain an initial mean solid fraction of $\langle \Theta_p \rangle \approx 0.45$, as shown in Figure 4a. Particle density is set to 2650kg/m^3 and the particle diameter distribution is lognormal with $d_{50} = 0.51$mm, $d_{max} = 0.75$mm, $d_{min} = 0.32$mm, $\sigma_g = 1.275$. The domain is periodic in the X and Z directions, with $L_x = 40d_{50}$ and $L_z = 20d_{50}$. Solid walls are located at $Y = \pm 30d_{50}$ for a total domain length of $L_y = 60d_{50}$.

During the initial phase of the simulation an additional solid wall is placed just below the particles at $Y = 0$, and they settle onto this boundary under the action of gravity in water for a total time of 5s (Figure 4b). At this point, Θ_{cp} is computed by integrating the solid volume of all particles in the interior of the packing, those which are more than $4d_{50}$ from the bottom wall or the top granular surface.

At $t = 5s$, the end sections of the solid wall, corresponding to a combined length of $L_X/4$, are removed, initiating an avalanche of particles into the bottom half of the

	d_{50}	σ_g	ρ_p	$v_{t,50}$	k_n	k_t	e_{dry}	St_c	St_e	$\mathcal{V}_s$	$\mathcal{V}_r$	Δt_p
Glass	0.35 mm	-	2500	48mm/s	1,000 N/m	400 N/m	0.65	11	130	0.15	0.0	1.5e-6 s
Sand	0.22 mm	1.35	2650	23mm/s	1,000 N/m	400 N/m	0.6	39	105	0.4	0.06	1.5e-6 s

TABLE 4. Particle and collision parameters used for the hindered settling tests.

container. This process is allowed to proceed until $t = 20s$ to ensure that all particles have settled completely. The angle of repose is then taken as the average of the four angles, $\phi_1, \phi_2, \phi_3, \phi_4$, produced by the avalanching process, shown in Figure 4c. To remove any influence of particle induced fluid motion on the static granular properties, a one-way coupling approach was used by setting $\Theta_p = 0$ and $\boldsymbol{f}_{p\to f} = 0$.

The test is repeated for 49 combinations of $\mathcal{V}_s$ and $\mathcal{V}_r$ ($\mathcal{V}_s$= 0.1, 0.2, 0.3, 0.4, 0.5, 0.6, 0.7 and $\mathcal{V}_r$ = 0.0, 0.02, 0.04, 0.06, 0.08, 0.10, 0.12). Other collision properties are held constant and are given in Table 3. Variation of the friction coefficients results in a considerable range of results ($0.57 \leq \Theta_{CP} \leq 0.63$, $20^o \leq \phi_r \leq 36^o$), which are shown in the in the $\mathcal{V}_s$-$\mathcal{V}_r$ plane in Figure 4d. The shaded region corresponds to results consistent with behavior of natural sand, which allows us to select $\mathcal{V}_s = 0.4$ and $\mathcal{V}_r = 0.06$ (marked by an X) for all subsequent simulations involving natural sand particles.

4.3. *Hindered Settling Dynamics*

A successful simulation of sediment dynamics in the wave bottom boundary layer must faithfully capture sediment-fluid interactions over a wide range of solid fractions, from very dilute to the close packed limit. In the present model, these interactions arise via the interphase momentum transfer term, the mixture viscosity and volume displacement effects. To confirm that the present combination of closures are consistent with known hindered settling behavior (Richardson & Zaki 1954), simulations of unbounded particle settling have been performed.

A triply periodic domain with $L_x = L_y = L_z = 64d_{50}$ is chosen for the simulations and discretized with 64^3 control volumes. Identical, non-overlapping particles are seeded at random to obtain mean solid fractions in the range $0.05 \leq \langle\Theta_p\rangle \leq 0.6$. Two sets of simulations are performed with uniform diameter glass beads ($d_p = 0.35$mm) and beach sand ($d_{50} = 0.22$mm, $\sigma_g = 1.35$), corresponding to the particle fluidization experiments of Baldock *et al.* (2004). Simulation parameters are given in Table 4. The particles are initially at rest and settle under the action of gravity ($g_y = -9.81$ ms^{-2}), while a uniform body force is applied to the fluid (water) in the positive y direction to balance the weight of the particles. The simulations last for $30\tau_d$, where $\tau_d = \frac{\rho_p d_{50}^2}{18\mu_0}$ is the Stokes relaxation time of the median grain size, long enough for the (average) settling velocity to achieve a stationary value.

In general the particles do not all settle at the same velocity because they induce an unsteady flow and form clusters of fast and slow moving particles as shown in Figure 5a for the case of glass beads at $\langle\Theta_p\rangle = 0.3$. Each particle is colored by its normalized settling velocity $v_s/v_{t,50}$, where $v_{t,50}$ is the unhindered terminal velocity of the median particle size. The normalized particle settling velocity (in a frame which the mean fluid velocity is zero) is averaged over all grains and plotted vs $\langle\Theta_p\rangle$ alongside the experimental data in Figure 5b. Also plotted is the empirical relationship of Richardson & Zaki (1954) for each condition. Overall, agreement with experiments is excellent over almost the entire range of solid fractions for both mono-size spherical particles as well as sand with a natural size distribution, indicating that the current set of closures are appropriate.

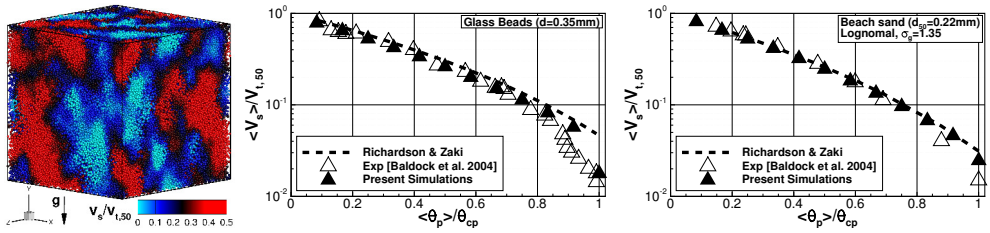

FIGURE 5. Hindered settling of a particle suspension under the action of gravity. (a) shows particles colored by instantaneous fall velocity for mean solid fraction, $\langle\Theta_p\rangle = 0.3$. (b) and (c) show average particle settling velocity normalized by the single particle terminal velocity, $v_{t,50}$, as a function of $\langle\Theta_p\rangle$. Comparisons are made with the Richardson & Zaki (1954) correlation, and the experimental measurements of Baldock *et al.* (2004).

Condition	VR	SF
Experimental Identifier	Mr5b63	MA5010
U_1 [m/s]	0.54	1.19
U_2 [m/s]	0.095	0.31
U_{max} [m/s]	0.64	1.50
a	0.59	0.63
T [s]	5	5
$\langle d_{50}\rangle$ [mm]	0.44	0.28
$\langle\sigma_g\rangle$	1.46	1.46
$v_{t,50}$[mm/s]	58	34
N_p	16.8M	3.6M
L_x [mm]	410	91
L_y [mm]	559	91
L_z [mm]	34	46
N_x	576	288
N_y	576	288
N_z	48	144
Δ [mm]	0.71	0.31
Δt_f [s]	1e-4	2.5e-5
Δt_p [s]	8.5e-7	4.3e-7

TABLE 5. Parameters used for oscillatory flow simulations.

5. Model application: Sand transport in oscillatory boundary layers

The remainder of this paper considers two simulations of sediment transport in oscillatory boundary layer flow, corresponding to condition Mr5b63 from the vortex ripple (VR) experiments of Van der Werf *et al.* (2007) and condition MA5010 from the sheet flow (SF) experiments of O'Donoghue & Wright (2004*a*,*b*). Both experiments were conducted in a closed loop, piston driven oscillatory flow tunnel and resulted in phase resolved velocity and concentration measurements.

5.1. *Simulation setup*

Table 5 provides an overview of the parameters used to setup these two simulations, and the numerical configuration is shown in Figure 6. In both experiments, the piston

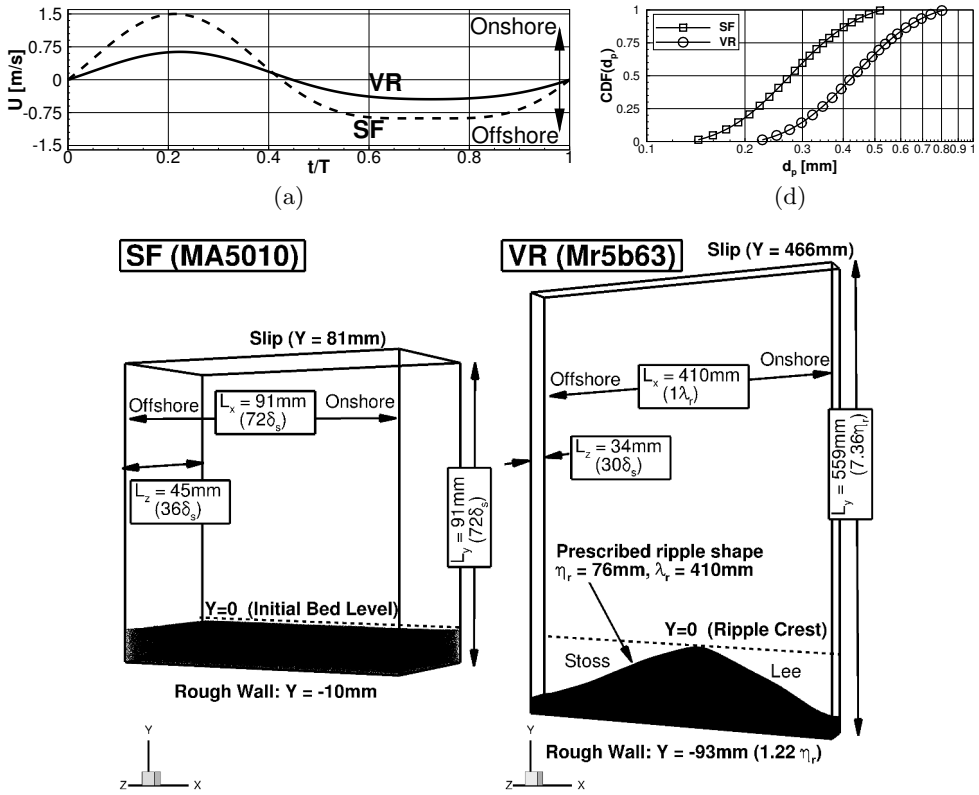

FIGURE 6. Setup of the mobile bed oscillatory flow simulations. (a) shows the free-stream velocity used to force the flow. (b) and (c) show the domain and initial particle configurations for the sheet flow and vortex ripple conditions respectively. (d) shows the particle size distributions used.

velocity, $U(t)$, corresponded to the near bed flow under a second order Stokes wave,

$$U(t) = u_1 \cos(\omega t - \gamma) + u_2 \cos(2\omega t - 2\gamma). \tag{5.1}$$

Here, $\omega = 2\pi/T$ is the angular frequency, T is the period, U_1 and U_2 are the first and second harmonic velocity amplitudes, and γ is the phase shift such that $U(0) = 0$,

$$\gamma = \arccos\left(\frac{\sqrt{U_1^2 + 8U_2^2} - U_1}{4U_2}\right). \tag{5.2}$$

$U(t)$ is shown in Figure 6a for both cases. Values of U_1 and U_2 were set so that the maximum free-stream velocity, U_{max}, was equal to 0.63 m/s in the vortex ripple condition and 1.50m/s in the sheet flow condition. Both cases have the same period, T, similar velocity asymmetry, $a = \frac{U_{max}}{U_{max} - U_{min}} \approx 0.6$, and similar moments of maximum onshore velocity ($t/T \approx 0.22$), maximum offshore velocity ($t/T \approx 0.72$), and flow reversal ($t/T \approx 0.44$). In the following results, positive values of $U(t)$ are considered to be "onshore" directed and negative values "offshore" directed.

The domains used in both simulations (shown in Figures 6b-c) were periodic in both the stream-wise (X) and span-wise (Z) direction. For the sheetflow case, the domain should be large enough in these directions that the velocity autocorrelation decays within half

the domain length, while in the wall normal (Y) direction the domain must be sufficiently tall to eliminate damping or generation of turbulence by the upper boundary. Salon *et al.* (2007) found that $L_x \gtrsim 50\delta_s$, $L_x \gtrsim 40\delta_s$ and $L_z \gtrsim 25\delta_s$ were sufficient to satisfy these conditions for smooth wall oscillatory flow simulations, where $\delta_s = \sqrt{\frac{\nu T}{\pi}}$ is the Stokes layer thickness. Taking into account the added thickness and roughness of our mobile bed, the domain for the sheet flow condition was chosen to be $L_x = 72\delta_s, L_y = 72\delta_s, L_z = 36\delta_s$. The domain for the rippled bed was made to be $L_x = 1\lambda_r, L_y = 6\eta_r, L_z = 30\delta_s$, where $\lambda_r = 0.41$ m and $\eta_r = 0.076$m are the experimentally measured ripple wavelength and amplitude. For any periodic rippled bed simulation L_x is constrained to be an integer multiple of the ripple wavelength, and in the present paper only a single ripple was simulated under the assumption that instantaneous hydrodynamics do not vary much from ripple to ripple. The span-wise thickness, $L_z = 30\delta_s$ was chosen to capture the near bed three dimensional hydrodynamics, but restricted major three dimensional morphological change. These are seen as reasonable first approximations for applying the model to rippled beds in light of the fact that the experimentally measured ripples were very uniform and two dimensional in the flow tunnel (Van der Werf *et al.* 2007). The upper slip boundary was located $L_y \approx 6\eta_r$ above the ripple crest corresponding to roughly the top of the flow tunnel. Both domains had an impenetrable bottom wall, made rough by fixing any particles which came into contact with it. The $Y = 0$ level was considered to be the initial bed level for the sheet flow condition and the ripple crest for the vortex ripple condition.

The sand used in both experiments was well sorted with medium grain sizes. A log-normal particle size distribution has been assumed, with geometric standard deviation of $\langle \sigma_g \rangle = 1.46$ for both conditions and median grain sizes, $\langle d_{50} \rangle$ equal to 0.28mm for the sheet flow condition and 0.44mm for the vortex ripple condition. The $\langle\ \rangle$ brackets here are used to distinguish these global properties from the local space-time dependent particle size distributions examined later on. Initial bed conditions were generated using the following procedure: First, the lognormal cumulative distribution functions (CDFs) shown in Figure 6b were sampled to obtain the diameter of individual particles. Then particles with these diameters were seeded in random non-overlapping positions in the lower portion of each domain. A total of $N_p = 3.8$M and 16.8M particles were employed for the sheet flow and vortex ripple simulations respectively. It was confirmed that the $\langle d_{10} \rangle$, $\langle d_{30} \rangle$, $\langle d_{50} \rangle$, $\langle d_{70} \rangle$, and $\langle d_{90} \rangle$ values of the particle populations closely matched the values reported in the experiments. The sand particles were allowed to settle under the action of gravity in water for several seconds until particle motion ceased. Finally, in the vortex ripple condition particles above the experimentally measured ripple surface were trimmed away to match the periodic ripple shape provided by Van der Werf *et al.* (2008). Due to the asymmetry of the flow this initial profile, shown in Figure 6d, is also asymmetric, with a steeper "lee" slope slope facing onshore and shallower "stoss" slope facing offshore. Particle collision parameters were set to the values used the natural sand simulations in Sections 4.2 and 4.3.

The continuous phase grid was uniform and cubic in the near bed region, with spacing of $\Delta = 0.71$ mm ($1.6d_{50}$) for the vortex ripple condition and $\Delta = 0.31$ mm ($1.1d_{50}$) for the sheet flow condition. To reduce the total number of control volumes somewhat, the vortex ripple grid was stretched in the vertical direction for $Y > 2.5\eta_r$, to a maximum spacing of $\Delta_{y,max} = 2.1$mm at the upper slip boundary. The resulting grids contain a total of 12M (sheet flow) and 16M (vortex ripple) control volumes.

After the initial beds are created, the flow was started from rest and a time dependent body force, representing the stream-wise oscillatory pressure gradient, was applied to

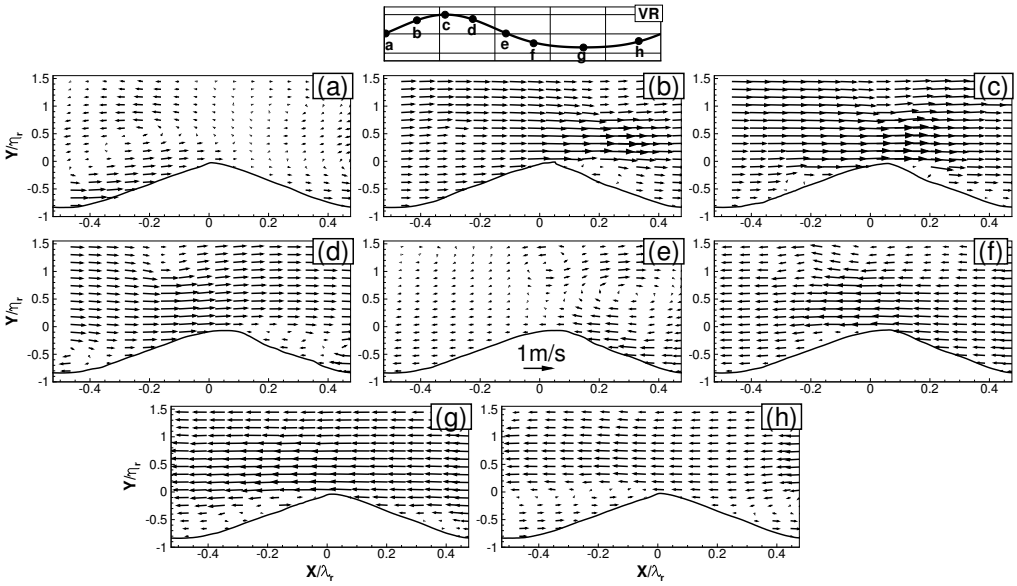

FIGURE 7. Spanwise and ensemble averaged 2D vector fields shown at selected phases for the vortex ripple case.

both the fluid and the particles.

$$F_x(t) = \rho_f \frac{dU(t)}{dt}. \tag{5.3}$$

A total of 4 cycles were simulated for the sheet flow condition, and 9 cycles for the vortex ripple condition. To minimize any morphological change due to startup effects in the vortex ripple case, all particles were held fixed for the first two cycles while the flow developed.

5.2. *Experimental validation*

To compare with the phase resolved experimental measurements, the simulation results have been averaged over the homogeneous directions (X and Z for sheet flow condition, Z for vortex ripple condition), and have been ensemble averaged over the final 3 cycles of each simulation.

5.2.1. *Near bed velocities*

Figure 7 shows the spanwise and ensemble averaged near-ripple fluid velocity vector fields at eight phases of the flow for the vortex ripple condition. The major features of the flow are consistent with the PIV results reported by Van der Werf *et al.* (2007) (not shown), which will briefly be summarize here: At the moments of flow reversal (a,e), a large vortex is ejected from the ripple trough. The vortex ejected over the lee slope at onshore reversal (e) is significantly stronger than the one ejected over the stoss slope during offshore reversal (a). This, combined with strong erosion of the ripple crest during the onshore half cycle (b,c,d) contributes to the asymmetric shape and onshore migration of the ripples. The overshoot of near bed flow velocity can be seen clearly during the acceleration and deceleration phases (b and f) above the ripple crest.

A direct comparison with near-ripple experimental measurements (PIV) is made in Figure 8 for eight points along the ripple. The data was extracted from points 9 mm above the simulated ripple surface (determined as the surface where $\Theta_p = 0.6$), corresponding as

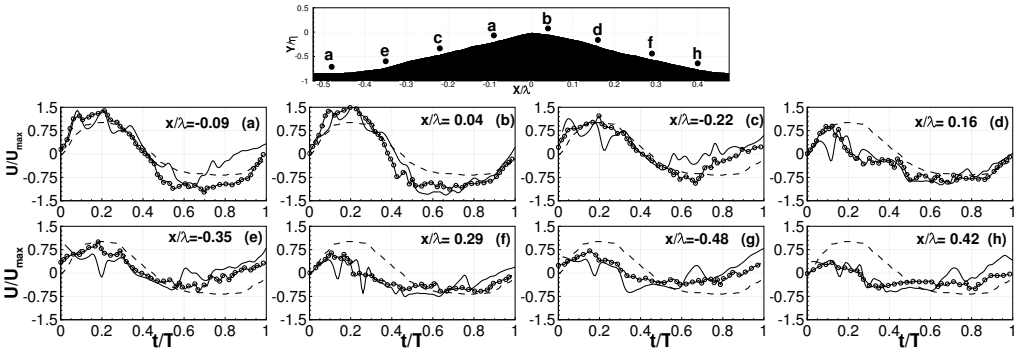

FIGURE 8. Comparison of predicted and measured velocities for the vortex ripple condition: — Simulation, ∘ Experiment (PIV), - - - Free stream velocity.

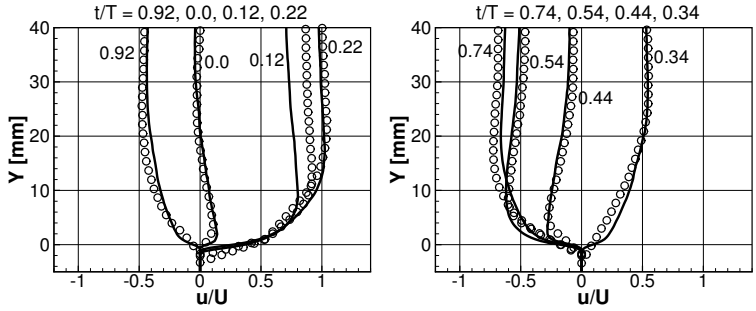

FIGURE 9. Comparison of predicted and measured velocities for the sheet flow condition: — Simulation, ∘ Experiment

closely as possible to the experiments. Overall, quite good agreement is achieved at most positions along the ripple. The maximum on and offshore velocities are very well predicted by the model, both above the crest and in the trough, indicating that vortex creation and ejection is well captured. The main disagreement can be found over the lee slope, shown in frames (a) and (c), during the creation of the stoss side vortex ($0.6 \lesssim t/T \lesssim 0.9$), which is possibly due to slight differences in the simulated and experimental ripple profile.

Figure 9 compares the measured and predicted velocity profiles at several phases for the sheet flow condition. The simulations capture the velocity skewness of the boundary layer, and agreement with the experimental measurements is quite good for all phases with the exception of the onshore acceleration (t/T=0.12) phase, which lags behind the measured profile. It is worth noting that due to three dimensional effects in the flow tunnel, the measured free-stream velocities are somewhat lower than the piston velocity used to drive the flow, and therefore exact hydrodynamic equivalence with the experiments is not achieved by forcing the flow using equation 5.1. However, the computed flow velocity profile follows the measured data very well from the fully packed bed up to the top of the suspension layer ($Y \approx 40$ mm), which indicates the good performance of the model across regions with a wide range of sediment concentrations.

5.2.2. *Suspended sediment concentrations*

The time and ripple-length (X) averaged suspended sediment concentrations predicted by the model are compared with the measurements in the left hand side of Figure 10 for the vortex ripple condition. The results show the characteristic exponential decay above the ripple crest (Nielsen 1992) and generally lie between the acoustic and optical

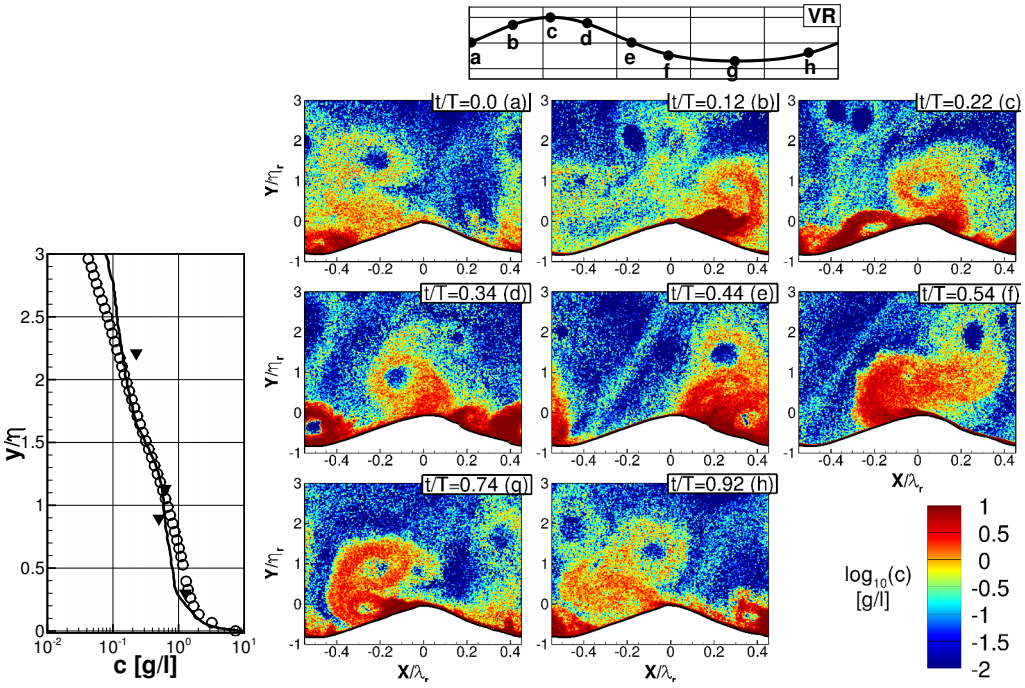

FIGURE 10. Suspended sediment concentrations for the vortex ripple condition. Figure at left shows the time and ripple averaged suspended sediment concentration as a function of height: — Simulation, ○ Experiment (acoustic), ▼ Experiment (optical). Contour plots on right show the ensemble averaged suspended sediment concentration at select phases ($\log_{10}$ scale).

measurements. Van der Werf *et al.* (2008) show a similar comparison based on two-dimensional advection-diffusion based models. The much larger discrepancies in their results were attributed to poorly predicted turbulence characteristics. A strength of the present model is that the time dependent concentration field depends only on Lagrangian particle motion with no uncertainties introduced to the concentration field through an advection-diffusion solution, reference concentration, or pickup function. The results also suggest that in addition to the turbulence, particle size effects may also plays a very important role in determining the cycle averaged concentration, as examined in the following section.

In the right hand side of Figure 10, the spanwise and ensemble averaged suspended sediment concentration fields are shown at several phases of the cycle: At off-onshore flow reversal (a), a suspended sediment cloud with moderate concentrations can be seen over the stoss side slope, while a smaller region of high concentration is seen in the trough. This sediment is carried over one or two ripple lengths as the flow accelerates onshore, with a certain amount of sediment settling back to the bed during this time (b,c). At the same time, the ripple crest is eroded by the strong onshore flow (b,c,d). As the flow begins to decelerate (d), there is abundant sediment in suspension along the lee side slope due to the lee vortex generation. The lee vortex is therefore very rich in suspended sediment when it is ejected around the time of on-offshore flow reversal, resulting in a large suspended sediment cloud over the ripple crest (e,f). This cloud passes through the periodic domain and over 3 crests at roughly t/T=0.5, t/T=0.7, and t/T=0.9, consistent with experimental observations.

The concentration profiles in the lower sheet flow layer are shown in Figure 11 for the

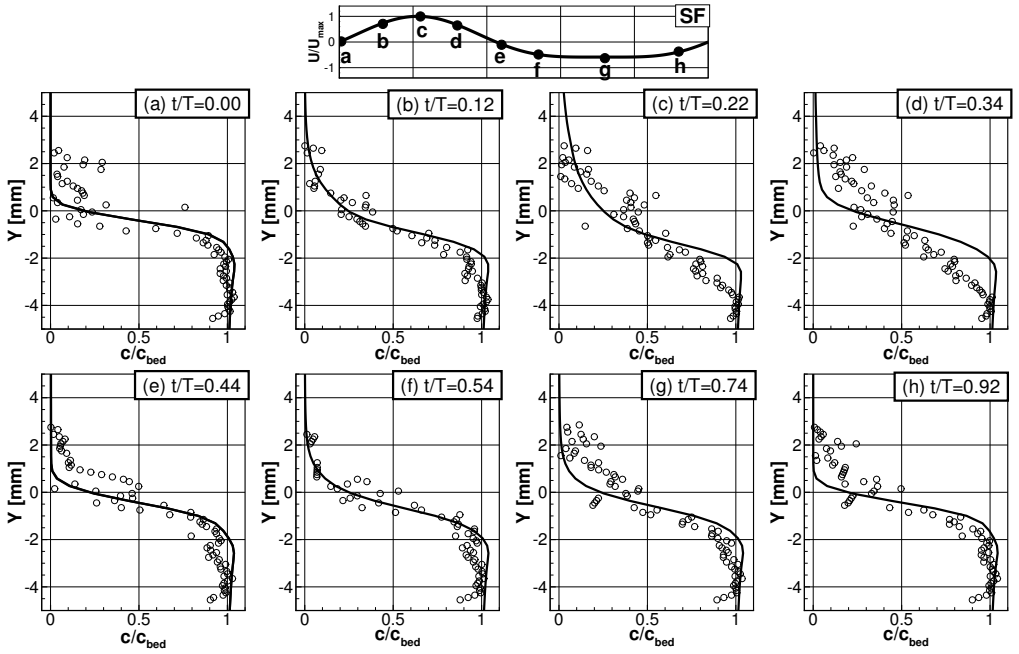

FIGURE 11. Sediment concentrations at select phases in the sheet flow layer: — Simulation, ∘ Experiment (CCM)

sheet flow condition, and compared with experimental measurements made using a conductivity concentration meter (CCM). Concentration measurements have been normalized by the undisturbed bed concentration ($c_{bed} \approx 1600$ g/l). The computed sediment concentration follows the CCM measurements very well in both pickup layer ($Y < -2$ mm) and upper sheet flow layer (-2 mm $<$ Y $<$ 2 mm). The main discrepancy seems to be around the initial deceleration towards on-offshore flow reversal (frames c and d), which suggests that the model under-predicts the pickup of sediment from the lower part of the bed at the maximum flow. The overall agreements, however, are considered to be very good, which indicates model's good capability in simulating particle-particle and fluid-particle interactions in such high concentration regions.

5.3. *Three dimensional description*

To this point streamwise and span-wise averaging have been used to reduce these flows to either one or two spatial dimensions (in addition to time). However, at the Reynolds numbers involved in the experiments, the turbulent structure of the flow and its interaction with the sediment are known to be highly three dimensional (Ozdemir *et al.* 2010; Penko *et al.* 2013). Of particular importance are the three dimensional vortical structures which provide the regions of upward directed flow necessary for sediment to travel away from the bed and remain in suspension. The swirling strength criteria of Zhou *et al.* (1999*a*) is used to extract these features and examine their interaction with the particle phase by plotting iso-surfaces of λ_{ci} along with instantaneous particle positions in Figures 12 and 13. To remove very small scale features from the visualizations, a low pass filter has been applied to the instantaneous velocity fields before computing $\nabla \boldsymbol{u}_f$ and its eigenvalues. To allow spatio-temporal size sorting to be identified, individual particles have been colored and rendered according to their size.

Figure 12 shows these results for the vortex ripple condition at eight phases of the

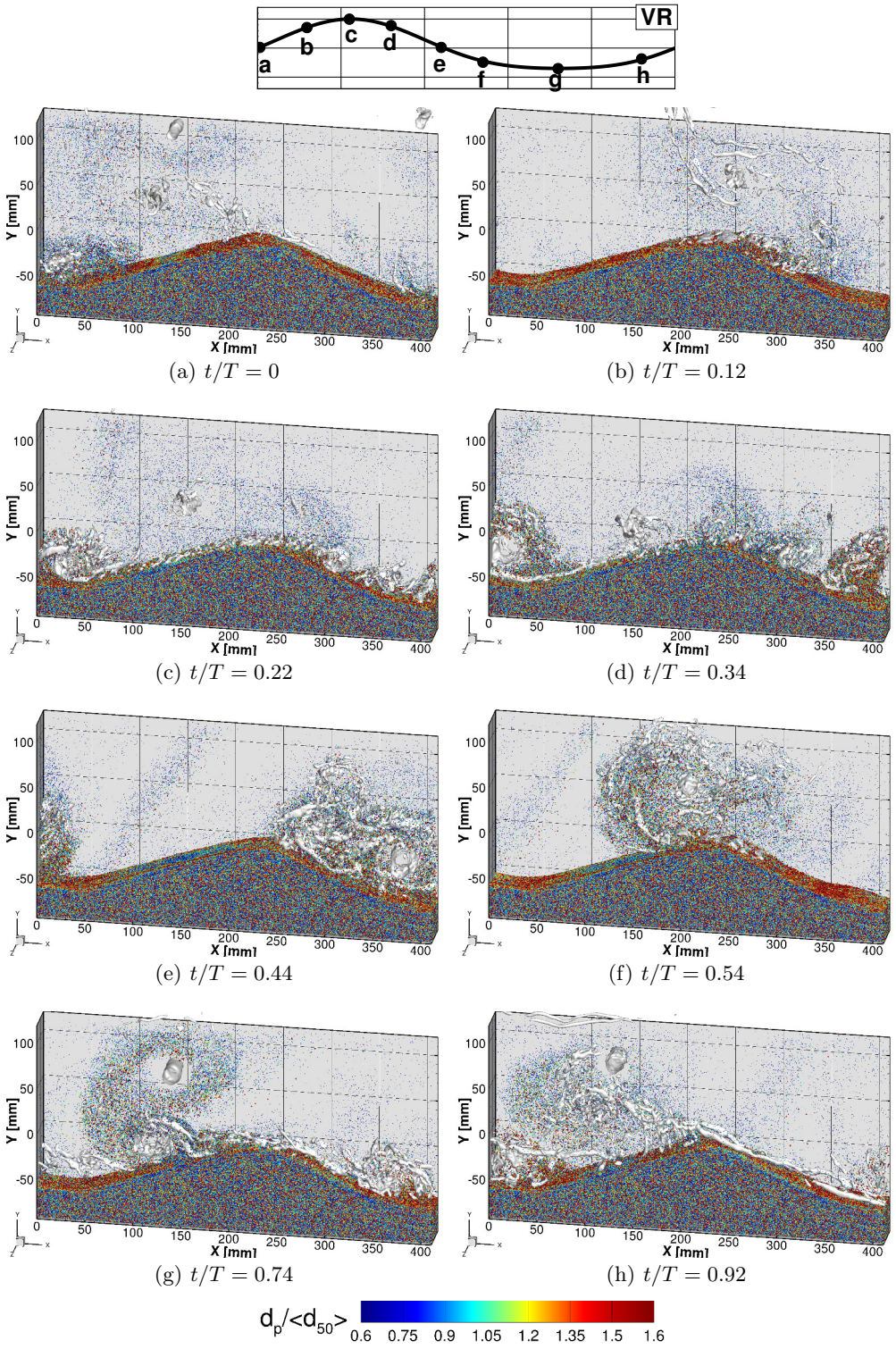

(a) $t/T = 0$ (b) $t/T = 0.12$

(c) $t/T = 0.22$ (d) $t/T = 0.34$

(e) $t/T = 0.44$ (f) $t/T = 0.54$

(g) $t/T = 0.74$ (h) $t/T = 0.92$

FIGURE 12. Three dimensional snapshots of vortex cores visualized as isosurfaces of $\lambda_{ci} = 20s^{-1}$ and particle positions at 8 phases of the oscillatory flow for the vortex ripple condition. Individual particles have been rendered at twice their actual size to aid in visualization.

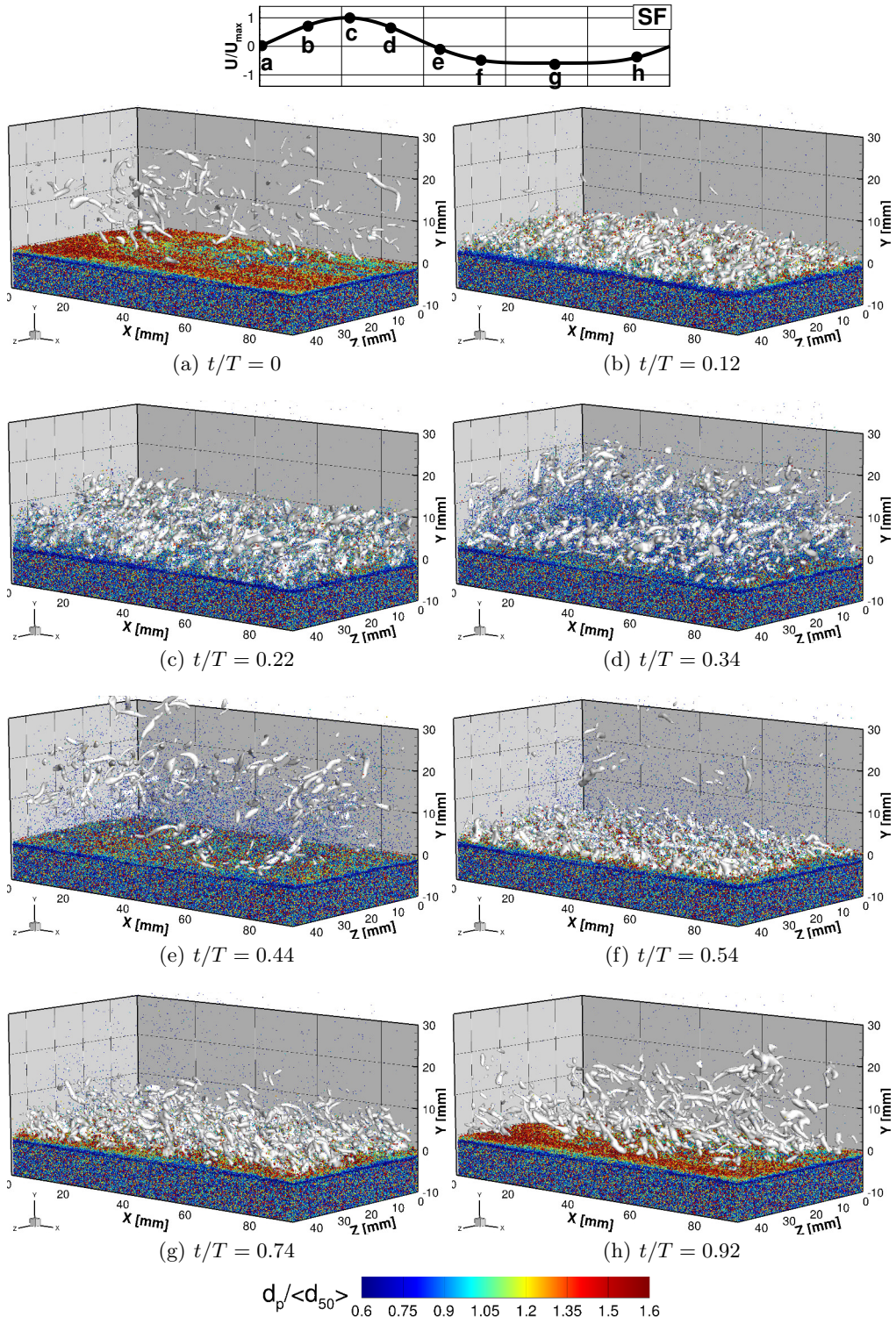

(a) $t/T = 0$ (b) $t/T = 0.12$

(c) $t/T = 0.22$ (d) $t/T = 0.34$

(e) $t/T = 0.44$ (f) $t/T = 0.54$

(g) $t/T = 0.74$ (h) $t/T = 0.92$

FIGURE 13. As in Figure 12, but for the sheet flow condition, with an isovalue of $\lambda_{ci} = 70s^{-1}$. Particles are rendered at their actual size.

wave cycle as in the previous section. The largest vortex cores can be seen to be pseudo-two dimensional, spanning the entire width of the domain in the Z direction. However, significant three dimensional, small scale structures are also evident throughout the cycle in the form of entangled vortex filaments around the larger two-dimensional vortex cores and streaks along the bed surface, similar to observations from other numerical studies (e.g. Vittori & Verzicco (1998); Scandura *et al.* (2000); Zedler & Street (2006); Schmeeckle (2014)). These coherent vortical features have a clear influence on particle motion throughout the cycle: At off-onshore flow reversal (a), a small vortex is detected at the bottom of the stoss slope in an area of high suspended sediment concentration (see also Figure 10a), also observed by Van der Werf *et al.* (2007). At the same time, remnants of several vortices ejected from the ripple trough during previous cycles can be seen higher in the water column, maintaining large amounts of particles around them. As the flow speed increases in the onshore direction (b), near bed vortical streaks appear around the crest, and as the flow separates over the lee slope, a number of particles are picked up by these near bed features. As the flow speed peaks (c), the 3D streaks cover the entire surface of the ripple, and some have rolled up into larger, pseudo-two dimensional vortex cores. Once the flow starts to reduce speed and reverse direction (d, e), these streaks are lifted from the bed and in the trough they roll up around a large two-dimensional vortex core, lifting a substantial amount of particles from the bed. This particle cloud extends as high as 100 mm above crest level as the lee vortex is ejected during flow reversal (e) and the flow accelerates offshore (f). During the offshore half cycle (e-h), a similar process takes place, but the near bed streaks have a longer time to develop and become more elongated along the ripple surface (g-h) due to the asymmetry of the wave.

Comparatively, the same results for the sheet flow conditions, shown in Figure 13, exhibit a lack of large scale vortex shedding, and more uniform near bed streaks that are significantly stronger (note the magnitude of the λ_{ci} isosurfaces is 3.5 times larger than in Figure 12). Similar to the vortex ripple condition, the flow is almost clear of vortical structures at the beginning of the cycle, apart from remnants of broken vortex cores from the last wave cycle. During the onshore flow acceleration (b, c), densely located, energetic vortical structures are generated close to the bed surface. These streaks remain close to the bed until maximum on-shore flow (c), and as the flow decelerates (d), they are lifted $10 - 20$ mm above the initial bed-level, carrying large quantities of particles with them. At on-offshore flow reversal (e), most the near bed streaks have been dissipated, although many of them remain higher in the water column. During the subsequent offshore half cycle (f-h) a similar process follows and, similarly to the vortex ripple condition, the near bed streaks become better developed and elongated due to the asymmetry of the mean flow.

5.4. *Behavior of different size fractions*

By rendering the particles according to size in Figures 12 and 13, strong spatio-temporal particle size sorting patterns are revealed, both near the bed and in suspension, which appear to be strongly influenced by the three dimensional flow field.

5.4.1. *Near the bed*

Throughout most of the wave cycle in the vortex ripple condition the bed surface is covered by large particles, and a similarly coarse surface layer can be seen at the low velocity phases under sheet flow conditions. The composition of this near bed surface layer is important, for it directly influences which particles are brought into suspension and at what phase of the cycle, thus influencing the net transport behavior (Dohmen-

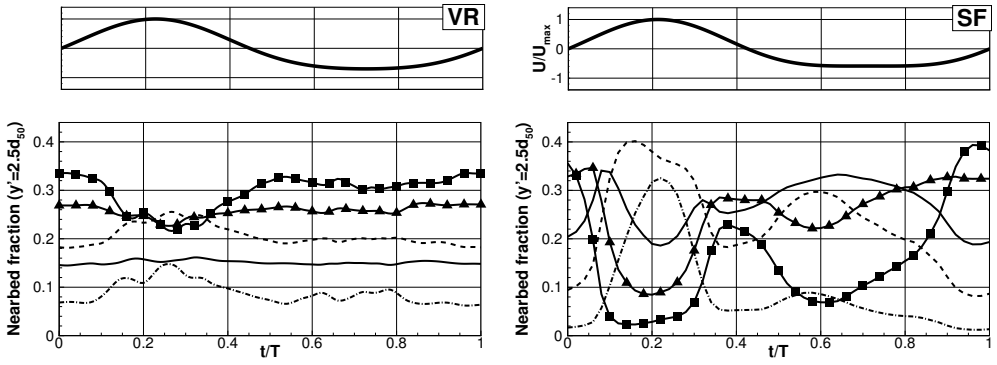

(a) Vortex Ripple (b) Sheet Flow

FIGURE 14. Relative abundance of different particle size fractions in the near bed layer, $Y' = Y_{bed} + 2.5d_{50}$: (-·-) d_{10}, (- - -) d_{30}, (—) d_{50}, (—▲—) d_{70}, (—■—) d_{90}

Janssen *et al.* 2002). This feature is explored in Figure 14, where the relative abundance of different particle sizes in the near bed layer, $Y' = Y_{bed}+2.5d_{50}$, has been plotted vs phase. To extract this result from the particle data, the instantaneous bed level, $Y_{bed}(x, z)$, is taken to be the local elevation where $\Theta_p = 0.6$, and particles are binned into 5 fractions with mean diameters, d_{10}, d_{30}, d_{50}, d_{70}, and d_{90}. In a perfectly mixed condition, each of these fractions would be expected to contribute 20% to the total composition. The departure of the results in Figure 14 from this behavior demonstrates the effectiveness of different flow driven particle size sorting mechanisms.

Under vortex ripple conditions, the composition of the near bed layer is nearly constant for the low velocity offshore half cycle, and is disproportionately coarse with roughly 2/3 of the solid volume being coarser than d_{60}. During onshore acceleration, when the near bed vortical streaks touch the bed surface (Figure 12 b-c), high speed flow near the bed is able to lift the coarse fractions into suspension. This exposes the finer fractions below, especially along the stoss side of the ripple, which experiences some of the largest near bed velocities (see Figure 8). Consequently, the particle sizes in the near bed layer are better mixed during the onshore half cycle and during formation of the lee vortex. When the lee vortex is ejected and passes over the crest (Figure 12 f & g), the largest fractions quickly settle down, coarsening the surface layer. Being exposed to the high velocities and vortical streaks for most of the cycle, the crest tends to lose coarse particles while the trough area is less affected by the streaks and hence accumulates the coarse fractions. Such a sorting process agrees with time averaged measurements of the settling velocity distribution (see Van der Werf *et al.* (2008) Figure 4). The near constant composition in the near bed layer reflects the fact that mixing and particle size sorting largely occur in the suspension under vortex ripple conditions, driven by large scale vortex shedding.

Under sheet flow conditions, the overall composition of the near bed layer is much more dynamic. A strong coarse-over-fine layering of particles is seen at low velocity phases (Figure 13 a,e), which results in a very coarse near bed composition. As the flow accelerates onshore, these coarse particles are lifted to a low level by the near bed streaks (Figure 13 b), and the layer composition changes from very coarse to very fine as the finer fractions below are mobilized around maximum onshore velocity (Figure 13 c). Once these fine fractions become exposed to the flow, they are rapidly brought into suspension by the near bed structures being lifted from the bed as the flow decelerates and reverses (Figure 13 d-e). At the point of flow reversal, the coarsest fractions have settled back to the bed and the near bed layer is again predominantly coarse. while many fine particles

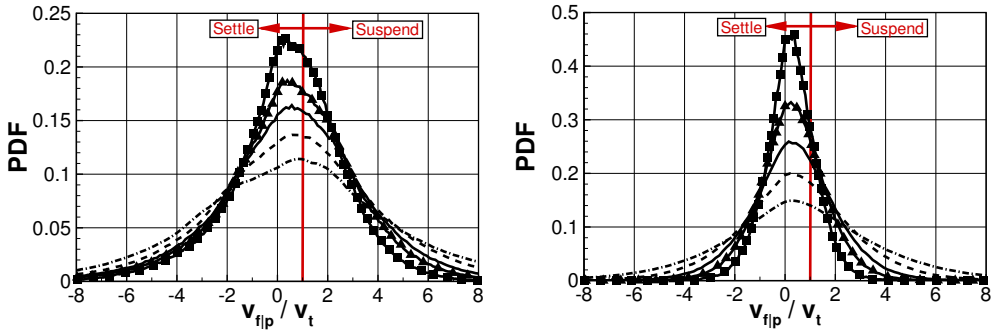

(a) Vortex Ripple (b) Sheet Flow

FIGURE 15. PDF of the vertical fluid velocity experienced by suspended particles ($\Theta_{p|p} < 0.08$) normalized by the clear water terminal settling velocity for five different size fractions in (a) the ripple bed condition (b) the sheet flow condition. (-·-) d_{10}, (- - -) d_{30}, (—) d_{50}, (—▲—) d_{70}, (—■—) d_{90}

remain in suspension. During the offshore half cycle (Figure 13f,g & h), the flow strength is low enough that the coarse particles remain close to the bed and only a small amount of fine particles are lifted into near bed suspension.

5.4.2. *In Suspension*

Once sediment is lifted from the bed, the three dimensional vortical structures provide the vertical velocities needed to retain particles in suspension. A net upward flux of particles can be achieved by a skewed vertical velocity probability (Bagnold 1966; Wei & Willmarth 1991) combined with a *loitering tendency* (Tooby *et al.* 1977; Nielsen 1992), which causes settling particles to spend more time sampling the upward parts of the flow against their downward settling preference. In Figure 15 the PDF of vertical fluid velocity experienced by suspended sediment particles ($\Theta_{p|p} < 0.08$) is plotted for both conditions. The vertical fluid velocities are normalized by the clear water terminal velocity for five different size fractions, so that the ratio $v_{f|p}/v_t > 1$ indicates fluid velocities resulting in upward particle suspension for each fraction, while $v_{f|p}/v_t < 1$ result in downward particle settling. In both conditions, the probability distributions are positively skewed, and have modes shifted to positive values of $v_{f|p}$. This shift in the mode decreases with particle sizes, and reflects the decreased potential of massive particles to become trapped in the vortical regions. In the vortex ripple condition, the mode of the vertical velocity distribution experienced by the smaller fractions corresponds to $v_{f|p}/v_t \approx 1$, underscoring the effectiveness of vortex trapping as a mechanism to retain sediment in suspension. This leads to the visible gradient in suspended particle sizes that will be explored in more detail in the next section.

5.5. *Spatio-temporal dynamics of the particle size distribution*

To better understand the grain size specific dynamics seen in Sections 5.3 and 5.4, the spatio-temporal dynamics of the particle-size distribution for these conditions are analyzed in Figure 16 as functions of vertical elevation, Y, and phase, t/T. (a) and (b) present the sediment concentrations. (c) and (d) show the ratio $d_{50}/\langle d_{50}\rangle$, which indicates the local mean particle size relative to the bed mean value, $\langle d_{50}\rangle$. (e) and (f) show the local σ_g value, which indicates the degree of mixing of the grain sizes. (g) and (h) show the mean volumetric settling velocity, $v_s = u_{p,y} - u_{f|p,y}$, normalized by $v_{t,50}$, the clear water terminal velocity of a particle with $d_p = \langle d_{50}\rangle$. Results were obtained by

streamwise and spanwise averaging over all particles at a given Y elevation. However, for the vortex ripple condition, only particles which have become entrained above the instantaneous bed-level ($\Theta_p < 0.08$) are included in the averages, thus the results are representative of the suspended particles in the vortex ripple condition. In all plots, the thick dashed line corresponds to the ripple crest in the vortex ripple condition or the initial bed level in the sheet flow condition.

Much of the suspension phenomena already discussed has clear signature in the space-time concentration plots (Figure 16 a-b). Significant sediment concentration, 1g/l or more, can be found under vortex ripple conditions up to as high as 120 mm ($1.5\eta_r$) above crest level throughout most of the cycle, with concentrations of 0.1g/l persisting up to 250mm above crest level ($3\eta_r$). In contrast, the majority of suspended sediment in the sheet flow condition is contained in the 30 mm above the initial bed level and there is significant settling of suspended particles during the low velocity phases. This again highlights the differences in sediment suspension mechanisms, and the effectiveness of the ripple generated turbulence at retaining sediment in suspension.

The parameters describing the particle size distribution demonstrate strong space-time dependence in these flows. In the vortex ripple condition, particles suspended in the high concentration regions below crest level are on average coarser than $\langle d_{50} \rangle$, due to the continuous pickup and settling of the coarse fractions from the ripple surface. The mean suspended particle size above the crest line bears resemblance to the concentration pattern: A significant rise in both concentration and d_{50} immediately after flow reversal (t/T = 0.4) at levels up to 100 mm is maintained until before the peak offshore flow (t/T = 0.7), due to the passage of the lee vortex sediment cloud. In this region, the particles are well mixed because the lee vortex is capable of lifting all particle sizes from the bed, and $\sigma_g \approx 1.35$ approaches the initial bed value (1.46) indicating the sediment cloud is well mixed. At elevations more than 100 mm above the crest, mean particle size is more or less constant at a given level throughout the cycle with values decreasing from $0.8\,\langle d_{50} \rangle$ at 100mm to $0.6\,\langle d_{50} \rangle$ at 300 mm. In this range, σ_g is also seen to decrease significantly, indicating that the sorting of particles by settling velocity is very effective. This is confirmed by Figure 16g, which shows a nearly constant vertical gradient of settling velocity above 100 mm.

The corresponding plots for the sheet flow condition reveal a very pronounced size sorting within the sheet flow layer. The most noticeable feature, which persists for the entire cycle and is also clearly visible in Figure 13, is a well-established layer of finer particles below the initial bed level. This layer develops very quickly (it is visible after just one flow cycle), and is armored by a layer of coarser particles above, consistent with the laboratory findings of Hassan & Ribberink (2005). During onshore acceleration, when the bed is rapidly mobilized, the high concentration sheet flow layer is very coarse up to the point of max velocity. It subsequently becomes progressively finer as the coarse particles are peeled away and the finer fractions become exposed to the flow. By the time flow reverses, the mean diameter in suspension is less than $0.85\,\langle d_{50} \rangle$, almost all the way down to the initial bed level. During the offshore half cycle, the sheet flow layer remains coarse because, as discussed in Section 5.3 and 5.4, the near bed flow is not energetic enough to expose the fine fractions below. During this time, a *particle mixing layer* (high σ_g) exists at the interface between the high and low concentration regions where coarse particles rising from the bed meet the fine particles left in suspension from the onshore half cycle. The variations in the fall velocity under sheet flow conditions reflect the functional dependence on particle size as well as local concentration and therefore vary significantly throughout the water column.

Within 100 mm of the crest in the vortex ripple condition, the temporal variation

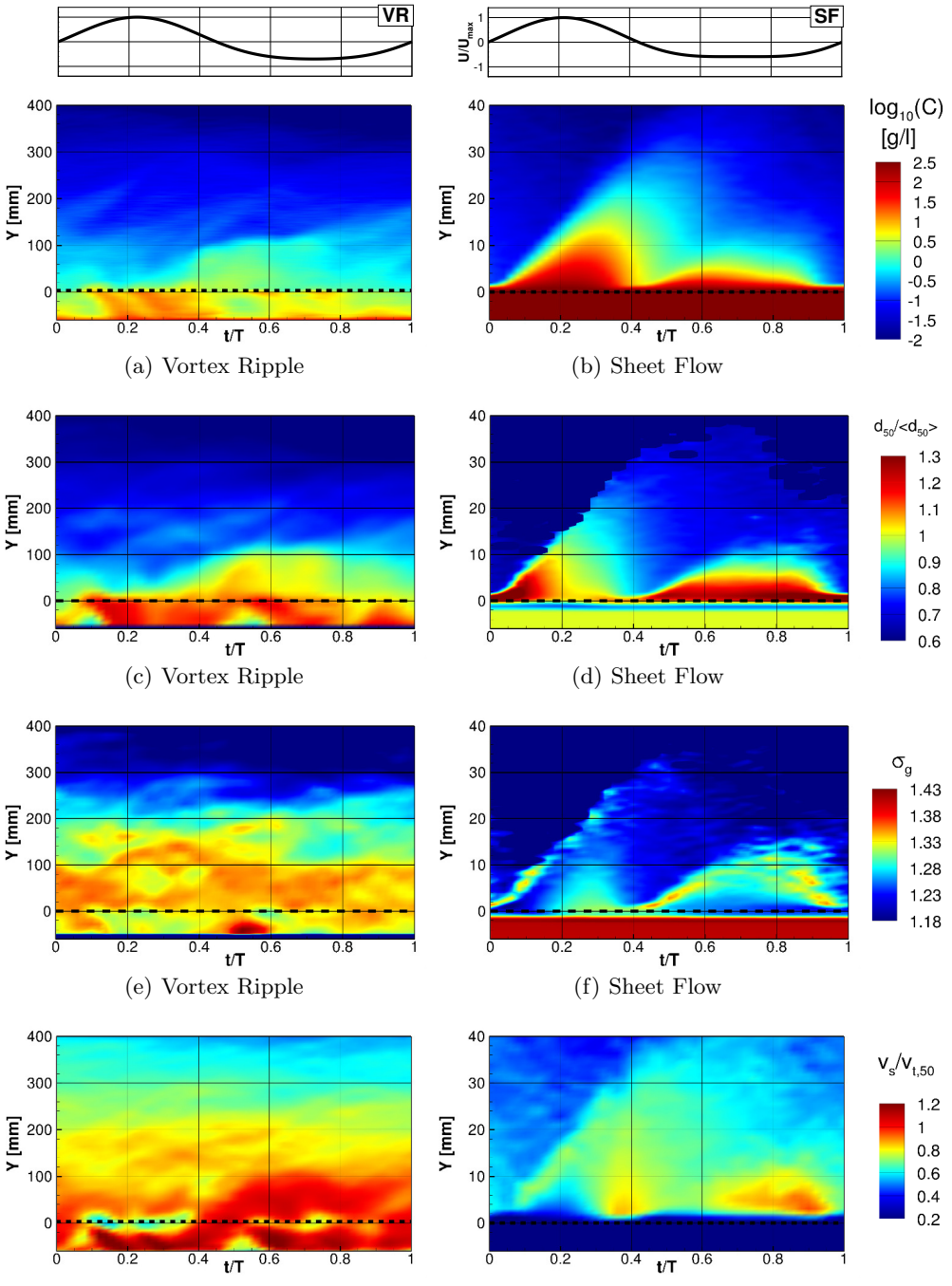

(a) Vortex Ripple (b) Sheet Flow

(c) Vortex Ripple (d) Sheet Flow

(e) Vortex Ripple (f) Sheet Flow

(g) Vortex Ripple (h) Sheet Flow

FIGURE 16. Space-time visualization of particle size distributions in the oscillatory boundary layer simulations. (a) and (b) show the time dependence of layer averaged concentration ($\log_{10}$ scale). (c) and (d) show the time dependence of layer averaged d_{50} normalized by $\langle d_{50} \rangle$. (e) and (f) show time dependence of layer averaged σ_g. (g) and (h) show the time dependence of layer averaged settling velocity, v_s, normalized by $v_{t,50}$, the terminal velocity of an isolated particle with $d = d_{50}$ The dashed line corresponds to the ripple crest (vortex ripple) or the initial bed level (sheet flow).

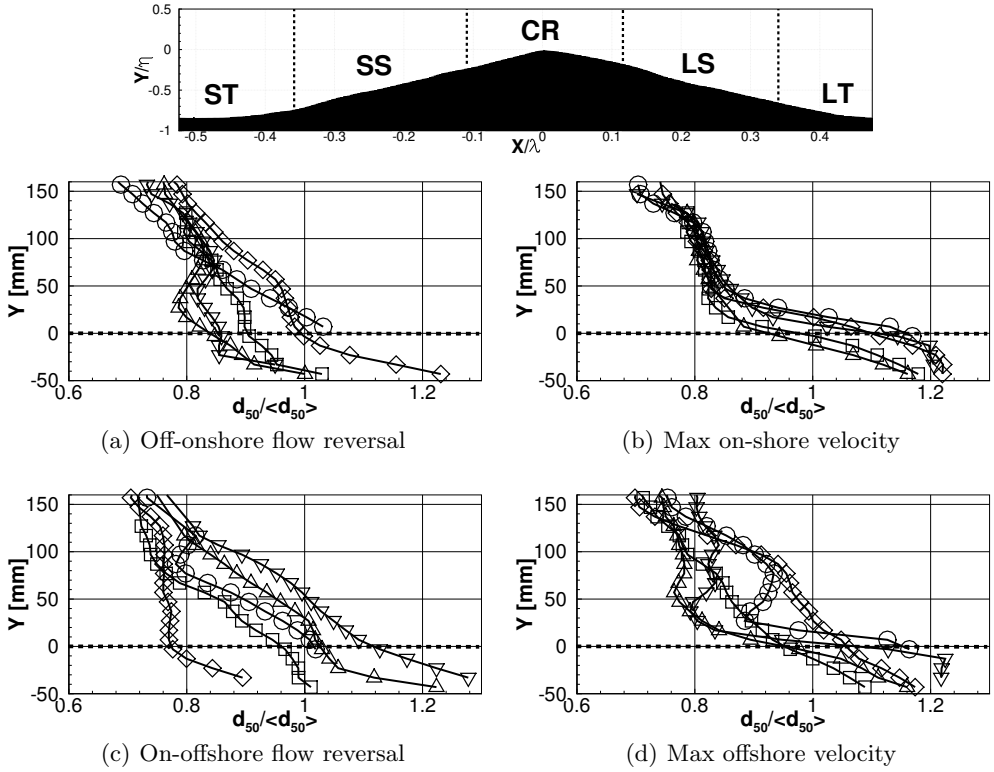

(a) Off-onshore flow reversal (b) Max on-shore velocity

(c) On-offshore flow reversal (d) Max offshore velocity

FIGURE 17. Vertical profiles of normalized local d_{50} at 4 different instances for the vortex ripple case. Each profile corresponds to one of the 5 zones shown above. (—□—) Stoss trough, (—◇—) Stoss slope, (—○—) Crest, (—∇—) Lee Slope, (—Δ—) Lee Trough.

of d_{50}, and σ_g is due to specific pickup, suspension, and transport events occurring in different lateral zones along the ripple. To better understand these dynamics, the vertical variation of d_{50} is plotted in Figure 17 at the moments of off-onshore flow reversal (a), peak onshore velocity (b), on-offshore flow reversal (c), and peak offshore velocity (d) for each of five lateral zones: the stoss side trough (ST), the stoss side slope (SS), the crest (CR), the lee side slope (LS) and the lee side trough (LT). The variability of d_{50} amongst different lateral zones is quite strong at the moments of flow reversal (a,c), when the energetic vortex ejection events entrain coarse particles from one side of the ripple surface, but on the opposite slope smaller particles are able to settle due to the low velocities. At these moments, the mean suspended particle size at a given vertical level in the ripple trough varies by almost 50%. There is comparably less lateral variation during the peak velocity phases (b,d) when turbulent advection/diffusion processes are dominant. At max onshore velocity (b), all vertical size profiles are similar, while at max offshore velocity, the signature of the coarse sediment cloud passing over the crest and lee slope can be seen between 50 and 100 mm above the crest.

5.6. *Collisional dynamics*

To model immersed particle impacts in the wave bottom boundary layer, it is common for both continuum and particle based approaches to use a single coefficient of normal restitution, e_n. For irregular particles with non-uniform sizes and conditions that result in spatio-temporal grain size sorting an obvious choice for this coefficient may not exist,

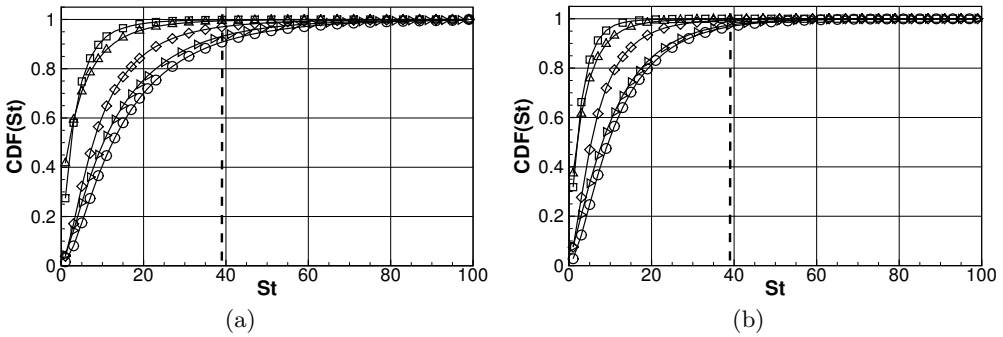

FIGURE 18. Time averaged cumulative distribution functions of the collisional Stokes number (Equation 3.2) for (a) vortex ripple conditions (b) sheet flow conditions. Individual CDFs are computed for collisions occurring in regions of different solid fractions: (—□—) $\Theta_p < 0.02$,(—◇—) $0.02 \leq \Theta_p < 0.08$, (—○—) $0.08 \leq \Theta_p < 0.2$, (—▷—) $0.2 \leq \Theta_p < 0.3$, (—△—) $0.3 \leq \Theta_p < 0.4$. The dashed line corresponds to $St = 39$, the threshold of zero rebound for natural sand grains found by Schmeeckle *et al.* (2001).

which is why the impact Stokes number is used to compute e_n on a per-collision basis. It is therefore of interest to examine the impact Stokes number statistics from the simulation data for these two cases. In Figure 18 the CDF of impact Stokes number (Equation 3.2) is plotted for both conditions. The different symbols correspond to collisions occurring in regions with different solid fractions. Also plotted as a dashed line is the $St = 39$ threshold for viscously damped rebound observed by Schmeeckle *et al.* (2001) for quartz sands. For both cases, at very low and high solid fractions, nearly all collisions occur at very low Stokes numbers, $\lesssim 20$. This is for different reasons: Low concentration regions ($\Theta_p < 0.02$) in these flows are higher in the water column and contain finer fractions in suspension. These fractions will have faster response times (low fall velocities), making the likelihood of an energetic collision due to large relative velocity between particles very small. Conversely, at very high solid fractions in and near the bed ($\Theta_p > 0.3$) relative particle motion is inhibited by much lower settling velocities, even for large particles. At intermediate solid fractions in the range $0.02 \leq \Theta_p \leq 0.3$, occurring in the sheet flow layer and the ripple trough, a broader range of St is observed for both conditions. However, most impacts occur well below the critical value of $St = 39$. In the vortex ripple case, which has a larger d_{50}, roughly 10% of all collisions percentage of collisions occur above this threshold.

These statistics indicate that using a small constant coefficient of normal restitution to mimic the viscous damping of low Stokes number impacts may be a safe assumption for small to medium size sand. For much larger particles however, caution should be taken because impact Stokes numbers will grow non-linearly with particle size. Also, in light of the strong particle size sorting effects observed in these flows, unphysically low restitution coefficients may result in a sink of energy for the larger particle fractions, or during energetic suspension events at particular phases of the flow.

6. Conclusions

An Euler-Lagrange point-particle model has been developed to simulate the dynamics of sub-aqueous natural sand particles. Several characteristics of the model allow it to faithfully reproduce the well known individual and collective behavior of natural sand grains, specifically:

(*a*) A variable model for the coefficient of normal restitution is used to model immersed particle-particle impacts. This allows the model to capture the dynamics of lubricated collisions at low and transitional impact Stokes numbers, as well as particle rebound of more massive particles involved in energetic collisions.

(*b*) A rolling friction model is combined with the typical sliding friction approach to capture the enhanced friction of angular natural sand grains. The frictional coefficients were calibrated to match the close packing fraction and angle of repose of natural quartz sands.

(*c*) The particle-fluid interactions, and crucially the drag law and the mixture viscosity model, implicitly take into account the effects of particle shape, particle concentration, and the local particle size distribution. This allows the model to reproduce the settling velocity behavior of both uniform spheres and angular sands for solid fractions ranging from dilute to close packed.

After systematically validating and calibrating the model, it was applied to simulate sand particle motion in asymmetric oscillatory flow conditions typical of the wave bottom boundary layer in both the vortex ripple and sheet flow regimes. Conditions were matched with the medium sand flow tunnel experiments of Van der Werf *et al.* (2007) and O'Donoghue & Wright (2004*a*,*b*), and predictions of phase resolved velocity and concentration fields are in overall excellent agreement with the experimental measurements. The three dimensional, phase resolved data were used to understand particle motion in these two very different conditions, and to characterize the flow induced particle size sorting. From these detailed particle based datasets the following conclusions can be drawn:

(*a*) Despite these flows being nominally one or two dimensional, the near bed vortical structures responsible for sediment pickup, suspension, and mixing, are highly three dimensional. In the vortex ripple condition the dominant flow features, detected with the λ_{ci} criteria, involve a pseudo two-dimensional core and a mass of entangled three-dimensional vortex filaments, usually accompanied by large sediment clouds. In the sheet flow condition, near bed vortical streaks are created during each half cycle, and bring significant amounts of sediment into suspension when they are lifted from the bed at flow reversal.

(*b*) Even for the fairly narrow particle size distributions considered here, strong sorting of the suspended sediment by particle size is significant under both sheet flow and vortex ripple conditions. The size sorting demonstrates significant space and time dependence due to the influence of specific suspension/settling events that lead to segregation and mixing of the grain size population.

(*c*) Both conditions show a strong inverse size gradation of particles in the surface layers, with a layer of the coarsest particles resting above the finer fractions at moments of low velocity. This armoring of the fine fractions restricts their vertical mobility and means that only the most energetic suspension events are able to suspend significant amounts of sediment due to the low mobility of the surface particles. This was quantified by examining the composition of the near bed layer, which is very different under these two conditions. In the vortex ripple case, this layer remains predominantly coarse throughout most of the cycle. The strong near bed vortical streaks and major disturbance of the bed by the lee vortex result in a mixing of all size fractions around maximum onshore velocity. In the sheet flow condition, the near bed layer composition is much more dynamic, and all fractions participate in the pickup events during different phases of the flow.

(*d*) There is a preference for suspended particles to sample upward velocity regions of the flow generated by three dimensional vortices. This is due to both a positively skewed velocity probability in the flow as well as a tendency of the particles to loiter in regions of

upward directed flow created by 3D vortices. In the vortex ripple conditions, the velocity of maximum probability is sufficient to keep the smaller fractions permanently suspended, enhancing the vertical size sorting of grains in suspension.

(e) For the medium size sands considered, most particle-particle impacts occur at low impact Stokes numbers, where lubrication forces can be expected to result in near or complete damping of rebound velocities. Some more energetic collisions do occur, especially in high concentration regions of the ripple trough, but it is expected that a low constant coefficient of restitution will yield satisfactory results when simulating fine to medium size sand with a spring-damper type model for normal collision force.

Acknowledgements

Financial support for JRF and ML was provided from the joint EPSRC/STW funded SINBAD project and is highly appreciated. SVA thanks NSF for support from project #1133363. This work used the ARCHER UK National Supercomputing Service (`http://www.archer.ac.uk`) as well as the Stampede system at the Texas Advanced Computing Center. We thank Professor Tom Baldock, Professor Tom O'Donoghue, and Dr Julian Simeonov for sharing experimental and numerical data with us. We thank Dr Andrew Cihonski for helpful comments on an early version of this manuscript.

This research has produced a data set containing detailed particle and fluid motions in oscillatory boundary layers. To enable the use of the data to contribute to new physical understanding sediment transport processes, a database hosted by the University of Liverpool is available at the website `http://datacat.liverpool.ac.uk/id/eprint/43`.

REFERENCES

Ahmed, Ahmed SM & Sato, Shinji 2003 A sheetflow transport model for asymmetric oscillatory flows: Part ii: Mixed grain size sediments. *Coastal Engineering Journal* **45** (03), 339–361.

Anderson, T Bo & Jackson, Roy 1967 Fluid mechanical description of fluidized beds. equations of motion. *Industrial & Engineering Chemistry Fundamentals* **6** (4), 527–539.

Bagnold, Ralph A 1954 Experiments on a gravity-free dispersion of large solid spheres in a newtonian fluid under shear. In *Proceedings of the Royal Society of London A: Mathematical, Physical and Engineering Sciences*, , vol. 225, pp. 49–63. The Royal Society.

Bagnold, Ralph Alger 1966 An approach to the sediment transport problem from general physics. *The Physics of Sediment Transport by Wind and Water: A Collection of Hallmark Papers by RA Bagnold* pp. 231–291.

Baldock, TE, Tomkins, MR, Nielsen, P & Hughes, MG 2004 Settling velocity of sediments at high concentrations. *Coastal engineering* **51** (1), 91–100.

Beetstra, R, Van der Hoef, MA & Kuipers, JAM 2007*a* Drag force of intermediate reynolds number flow past mono-and bidisperse arrays of spheres. *AIChE Journal* **53** (2), 489–501.

Beetstra, R, Van der Hoef, MA & Kuipers, JAM 2007*b* Erratum to "drag force of intermediate reynolds number flow past mono-and bidisperse arrays of spheres". *AIChE Journal* **53** (2), 489–501.

Black, Kerry P & Oldman, John W 1999 Wave mechanisms responsible for grain sorting and non-uniform ripple distribution across two moderate-energy, sandy continental shelves. *Marine Geology* **162** (1), 121–132.

Blondeaux, Paolo 2012 Sediment mixtures, coastal bedforms and grain sorting phenomena: An overview of the theoretical analyses. *Advances in Water Resources* **48**, 113–124.

Brendel, L & Dippel, S 1998 Lasting contacts in molecular dynamics simulations. In *Physics of dry granular media*, pp. 313–318. Springer.

Calantoni, J, Holland, KT & Drake, TG 2004 Modelling sheet-flow sediment transport in

wave-bottom boundary layers using discrete-element modelling. *Philosophical transactions. Series A, Mathematical, physical, and engineering sciences* **362** (1822), 1987.

Camenen, Benoît & Larson, Magnus 2006 Phase-lag effects in sheet flow transport. *Coastal engineering* **53** (5), 531–542.

Capecelatro, Jesse & Desjardins, Olivier 2012 An Euler-Lagrange strategy for simulating particle-laden flows. *Journal of Computational Physics* .

Cihonski, Andrew J, Finn, Justin R & Apte, Sourabh V 2013 Volume displacement effects during bubble entrainment in a travelling vortex ring. *Journal of Fluid Mechanics* **721**, 225–267.

Cundall, Peter A & Strack, Otto DL 1979 A discrete numerical model for granular assemblies. *Geotechnique* **29** (1), 47–65.

Deen, Niels G, van Sint Annaland, M & Kuipers, JAM 2004 Multi-scale modeling of dispersed gas–liquid two-phase flow. *Chemical Engineering Science* **59** (8), 1853–1861.

Derksen, JJ 2011 Simulations of granular bed erosion due to laminar shear flow near the critical shields number. *Physics of Fluids (1994-present)* **23** (11), 113303.

Dohmen-Janssen, C Marjolein, Kroekenstoel, David F, Hassan, Wael N & Ribberink, Jan S 2002 Phase lags in oscillatory sheet flow: experiments and bed load modelling. *Coastal Engineering* **46** (1), 61–87.

Drake, Thomas G & Calantoni, Joseph 2001 Discrete particle model for sheet flow sediment transport in the nearshore. *Journal of Geophysical Research: Oceans (1978–2012)* **106** (C9), 19859–19868.

Egiazaroff, IV 1965 Calculation of nonuniform sediment concentrations. In *Proc. ASCE*, , vol. 91, pp. 225–247.

Eilers, H 1941 The viscosity of the emulsion of highly viscous substances as function of concentration. *Kolloid-Zeitschrift* **97** (3), 313–321.

Finn, Justin, Shams, Ehsan & Apte, Sourabh V 2011 Modeling and simulation of multiple bubble entrainment and interactions with two dimensional vortical flows. *Physics of Fluids* **23** (2), 023301–023301.

Fredsøe, Jørgen, Andersen, Ken H & Sumer, B Mutlu 1999 Wave plus current over a ripple-covered bed. *Coastal Engineering* **38** (4), 177–221.

Fredsøe, Jørgen, Deigaard, Rolf *et al.* 1992 *Mechanics of coastal sediment transport*, , vol. 3.

Hajivalie, Fatemeh, Yeganeh-Bakhtiary, Abbas, Houshanghi, Hamid & Gotoh, Hitoshi 2012 Euler–lagrange model for scour in front of vertical breakwater. *Applied Ocean Research* **34**, 96–106.

Hassan, WNM & Ribberink, JS 2010 Modelling of sand transport under wave-generated sheet flows with a rans diffusion model. *Coastal Engineering* **57** (1), 19–29.

Hassan, Wael N & Ribberink, Jan S 2005 Transport processes of uniform and mixed sands in oscillatory sheet flow. *Coastal Engineering* **52** (9), 745–770.

Hsu, Tian-Jian, Jenkins, James T & Liu, Philip L-F 2004 On two-phase sediment transport: sheet flow of massive particles. *Royal Society of London Proceedings Series A* **460**, 2223–2250.

Ji, C, Munjiza, A, Avital, E, Ma, J & Williams, JJR 2013 Direct numerical simulation of sediment entrainment in turbulent channel flow. *Physics of Fluids (1994-present)* **25** (5), 056601.

Jiang, Z & Haff, PK 1993 Multiparticle simulation methods applied to the micromechanics of bed load transport. *Water resources research* **29** (2), 399–412.

Joseph, GG, Zenit, R, Hunt, ML & Rosenwinkel, AM 2001 Particle–wall collisions in a viscous fluid. *Journal of Fluid Mechanics* **433**, 329–346.

Kidanemariam, Aman G & Uhlmann, Markus 2014*a* Direct numerical simulation of pattern formation in subaqueous sediment. *Journal of Fluid Mechanics* **750**, R2.

Kidanemariam, Aman G & Uhlmann, Markus 2014*b* Interface-resolved direct numerical simulation of the erosion of a sediment bed sheared by laminar channel flow. *International Journal of Multiphase Flow* **67**, 174–188.

Kranenburg, Wouter M, Hsu, Tian-Jian & Ribberink, Jan S 2014 Two-phase modeling of sheet-flow beneath waves and its dependence on grain size and streaming. *Advances in water resources* **72**, 57–70.

Legros, François 2002 Can dispersive pressure cause inverse grading in grain flows? *Journal of Sedimentary Research* **72** (1), 166–170.

Li, Ming & O'Connor, B. A. 2007 Numerical study of sediment transport above rippled beds under the action of combined waves and currents. *Sedimentology* **54** (6), 1345–1363.

Malarkey, J & Davies, AG 2002 Discrete vortex modelling of oscillatory flow over ripples. *Applied Ocean Research* **24** (3), 127–145.

Maxey, Martin R & Riley, James J 1983 Equation of motion for a small rigid sphere in a nonuniform flow. *Physics of Fluids (1958-1988)* **26** (4), 883–889.

Nielsen, Peter 1992 *Coastal bottom boundary layers and sediment transport*, , vol. 4. World scientific.

O'Donoghue, Tom & Wright, Scott 2004*a* Concentrations in oscillatory sheet flow for well sorted and graded sands. *Coastal Engineering* **50** (3), 117–138.

O'Donoghue, Tom & Wright, Scott 2004*b* Flow tunnel measurements of velocities and sand flux in oscillatory sheet flow for well-sorted and graded sands. *Coastal Engineering* **51** (11), 1163–1184.

Ozdemir, Celalettin E, Hsu, Tian-Jian & Balachandar, S 2010 A numerical investigation of fine particle laden flow in an oscillatory channel: the role of particle-induced density stratification. *Journal of Fluid Mechanics* **665**, 1–45.

Pan, Yingkang, Tanaka, Toshitsugu & Tsuji, Yutaka 2001 Direct numerical simulation of particle-laden rotating turbulent channel flow. *Physics of Fluids* **13**, 2320.

Patankar, NA & Joseph, DD 2001 Lagrangian numerical simulation of particulate flows. *International Journal of Multiphase Flow* **27** (10), 1685–1706.

Penko, AM, Calantoni, J, Rodriguez-Abudo, S, Foster, DL & Slinn, DN 2013 Three-dimensional mixture simulations of flow over dynamic rippled beds. *Journal of Geophysical Research: Oceans* **118** (3), 1543–1555.

Penko, Allison M, Calantoni, Joseph & Slinn, Donald N 2009 *Mixture theory model sensitivity to effective viscosity in simulations of sandy bedform dynamics*. IEEE.

Penko, Allison M, Slinn, Donald N & Calantoni, Joseph 2010 Model for mixture theory simulation of vortex sand ripple dynamics. *Journal of Waterway, Port, Coastal, and Ocean Engineering* **137** (5), 225–233.

Pöschel, Thorsten & Schwager, Thomas 2005 *Computational granular dynamics: models and algorithms*. Springer Science & Business Media.

Richardson, JF & Zaki, WN 1954 The sedimentation of a suspension of uniform spheres under conditions of viscous flow. *Chemical Engineering Science* **3** (2), 65–73.

van Rijn, Leonardus Cornelis 1993 *Principles of sediment transport in rivers, estuaries and coastal seas*, , vol. 1006. Aqua publications Amsterdam.

van Rijn, Leo C, Ribberink, Jan S, Werf, Jebbe Van Der & Walstra, Dirk JR 2013 Coastal sediment dynamics: recent advances and future research needs. *Journal of hydraulic research* **51** (5), 475–493.

Roos, Pieter C, Wemmenhove, Rik, Hulscher, Suzanne JMH, Hoeijmakers, Harry WM & Kruyt, NP 2007 Modeling the effect of nonuniform sediment on the dynamics of offshore tidal sandbanks. *Journal of Geophysical Research: Earth Surface (2003–2012)* **112** (F2).

Saffman, PGt 1965 The lift on a small sphere in a slow shear flow. *Journal of fluid mechanics* **22** (02), 385–400.

Salon, S, Armenio, V & Crise, A 2007 A numerical investigation of the stokes boundary layer in the turbulent regime. *Journal of Fluid Mechanics* **570**, 253–296.

Scandura, P, Vittori, G & Blondeaux, P 2000 Three-dimensional oscillatory flow over steep ripples. *Journal of Fluid Mechanics* **412**, 355–378.

Schiller, L. Naumann, Z. 1935 A drag coefficient correlation. *Ver. Deutsch. Ing.* pp. 77–318.

Schmeeckle, Mark W 2014 Numerical simulation of turbulence and sediment transport of medium sand. *Journal of Geophysical Research: Earth Surface* **119** (6), 1240–1262.

Schmeeckle, Mark W, Nelson, Jonathan M, Pitlick, John & Bennett, James P 2001 Interparticle collision of natural sediment grains in water. *Water Resources Research* **37** (9), 2377–2391.

Shams, E, Finn, J & Apte, SV 2011 A numerical scheme for euler–lagrange simulation of

bubbly flows in complex systems. *International Journal for Numerical Methods in Fluids* **67** (12), 1865–1898.

Simeonov, Julian A & Calantoni, Joseph 2012 Modeling mechanical contact and lubrication in direct numerical simulations of colliding particles. *International Journal of Multiphase Flow* **46**, 38–53.

Soulsby, Richard 1997 *Dynamics of marine sands: a manual for practical applications*. Thomas Telford.

Tang, Y, Peters, EAJF, Kuipers, JAM, Kriebitzsch, SHL & Hoef, MA 2014 A new drag correlation from fully resolved simulations of flow past monodisperse static arrays of spheres. *AIChE Journal* .

Tenneti, S, Garg, R & Subramaniam, S 2011 Drag law for monodisperse gas–solid systems using particle-resolved direct numerical simulation of flow past fixed assemblies of spheres. *International journal of multiphase flow* **37** (9), 1072–1092.

Tooby, Paul F, Wick, Gerald L & Isaacs, John D 1977 The motion of a small sphere in a rotating velocity field: a possible mechanism for suspending particles in turbulence. *Journal of Geophysical Research* **82** (15), 2096–2100.

Van der Hoef, MA, van Sint Annaland, M, Deen, NG & Kuipers, JAM 2008 Numerical simulation of dense gas-solid fluidized beds: a multiscale modeling strategy. *Annu. Rev. Fluid Mech.* **40**, 47–70.

Van der Werf, JJ, Doucette, JS, O'Donoghue, T & Ribberink, JS 2007 Detailed measurements of velocities and suspended sand concentrations over full-scale ripples in regular oscillatory flow. *Journal of Geophysical Research* **112** (F2), F02012.

Van der Werf, JJ, Magar, V, Malarkey, J, Guizien, K & ODonoghue, T 2008 2dv modelling of sediment transport processes over full-scale ripples in regular asymmetric oscillatory flow. *Continental Shelf Research* **28** (8), 1040–1056.

Vincent, CE, Stolk, A & Porter, CFC 1998 Sand suspension and transport on the middelkerke bank (southern north sea) by storms and tidal currents. *Marine Geology* **150** (1), 113–129.

Vittori, G & Verzicco, R 1998 Direct simulation of transition in an oscillatory boundary layer. *Journal of Fluid Mechanics* **371**, 207–232.

Wei, T & Willmarth, WW 1991 Examination of v-velocity fluctuations in a turbulent channel flow in the context of sediment transport. *Journal of Fluid Mechanics* **223**, 241–252.

Yang, F-L & Hunt, ML 2006 Dynamics of particle-particle collisions in a viscous liquid. *Physics of Fluids (1994-present)* **18** (12), 121506.

Zedler, Emily A & Street, Robert L 2006 Sediment transport over ripples in oscillatory flow. *Journal of Hydraulic Engineering* **132** (2), 180–193.

Zhou, Jigen, Adrian, Ronald J, Balachandar, S & Kendall, TM 1999*a* Mechanisms for generating coherent packets of hairpin vortices in channel flow. *Journal of Fluid Mechanics* **387**, 353–396.

Zhou, YC, Wright, BD, Yang, RY, Xu, BH & Yu, AB 1999*b* Rolling friction in the dynamic simulation of sandpile formation. *Physica A: Statistical Mechanics and its Applications* **269** (2), 536–553.